THE BELL SYSTEM TECHNICAL JOURNAL
Vol. 56, No. 1, January 1977
Printed in U.S.A.

Propagation of High-Frequency Elastic Surface Waves Along Cylinders With Various Cross-Sectional Shapes

By J. A. MORRISON, J. B. SEERY, and L. O. WILSON

(Manuscript received March 24, 1976)

Elastic surface waves, or Rayleigh waves, are disturbances that travel over the stress-free surface of an elastic solid, and whose amplitudes decay rapidly with depth into the solid. Earlier mathematical results are used to study numerically the properties of these waves on specific cylindrical objects that might be used as acoustic topographic waveguides. The lowest-order mode is investigated for cylinders with strictly nonconstant curvature. Mode confinement and its dependence on such things as cylinder shape and the value of the frequency parameter are studied. Phase and group velocities are also computed. Mode behavior is studied in the transition region between the case of cross-sectional boundary curves of nonconstant (and not "almost" constant) curvature, for which the modes are localized, and the case of constant curvature, for which they are not localized. Some higher-order modes are investigated for the rounded wedge.

I. INTRODUCTION

Elastic surface waves, or Rayleigh waves, are disturbances that travel over the stress-free surface of an elastic solid, and whose amplitudes decay rapidly with depth into the solid. In a series of earlier papers,[1–3] we developed and applied some mathematical techniques to describe the propagation of high-frequency elastic surface waves along cylinders of general cross section. Our intent was to learn more about the properties of such waves traveling down cylindrical objects that might be used as acoustic topographic waveguides. In this paper, we use our earlier mathematical results to study numerically the properties of elastic surface waves on certain specific cylindrical objects of interest. We treat

cylinders roughly corresponding to an elliptical bore, an elliptical rod, a wedge with a rounded tip, and a flat plane with a rounded ridge on it. The elastic medium is assumed to be homogeneous and isotropic.

The earlier papers discussed two approximate high-frequency descriptions of the surface-wave behavior: an asymptotic approximation and one which we termed a surface-wave approximation. The analysis involved a scalar wave equation, a vector wave equation, and rather complicated boundary conditions. Since the analysis was cumbersome, a simpler scalar "model problem" was first investigated by Morrison.[1] The techniques he developed had counterparts in the full elastic problem, which was treated by Wilson and Morrison[2] in the high-frequency asymptotic approximation, designated by A (as depicted in Fig. 1). The lowest-order surface-wave mode was investigated in almost as much detail as that for the scalar problem, but because of the algebraic complexities, the higher-order modes were less completely analyzed.

For the scalar problem,[1] Morrison had also obtained a surface-wave approximation describing the high-frequency behavior of the surface-wave modes. He then derived the analogous approximate equations for the high-frequency behavior of the elastic surface-wave modes.[3] Unlike

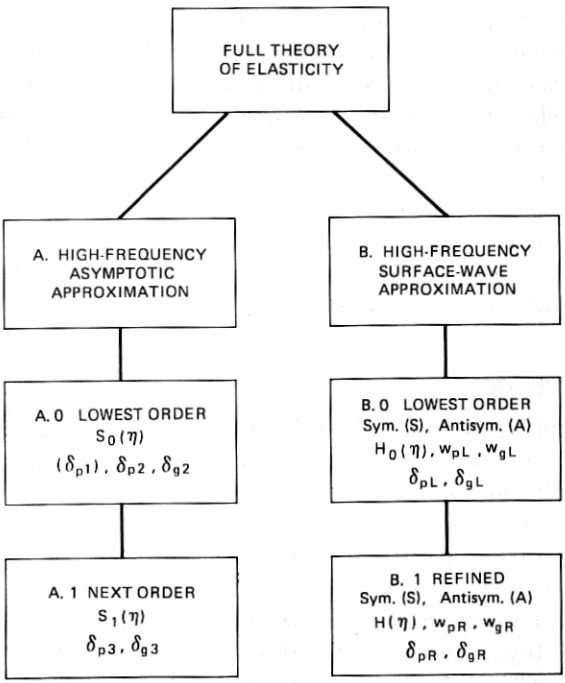

Fig. 1—High-frequency approximation chart.

the asymptotic approximation, A in Fig. 1, the surface-wave approximation, designated by B in Fig. 1, was capable of describing the mode behavior at high frequencies in the transition region between the case of cross-sectional boundary curves of nonconstant (and not "almost" constant) curvature, for which the modes are localized, and the case of constant curvature, for which they are not localized. (The asymptotic approximations had required boundary curves with strictly nonconstant curvature.) Also, this description gave a more complete analysis of the higher-order modes.

In Section II, we exhibit the cross-sectional boundary curvature functions used in our numerical investigations and explain why we chose those specific functions.

Section III is devoted to a numerical treatment of the high-frequency asymptotic results. The lowest-order mode is investigated for cylinders with strictly nonconstant curvature. We learn about the phenomenon of mode confinement, and its dependence upon such things as the shape of the cylinder and the value of the high-frequency parameter χ used in the asymptotic expansions, A in Fig. 1. We also compute the phase and group velocities.

In Section IV we make a similar investigation using the surface-wave approximation, B in Fig. 1. When possible, the results are compared with the asymptotic results. Particular attention is paid to the mode behavior in the transition region described earlier, and to the behavior of higher-order modes. We also compare our results with exact theoretical results for the circular bore.[4]

In Section V, we summarize our findings.

II. THE BOUNDARY CURVES

We wished to investigate numerically the properties of disturbances propagating along the surfaces of various cylindrical objects. The motivation for our particular choices of cross-sectional boundary curves came from our earlier high-frequency asymptotic results,[2] which could be applied to a cylinder with an open boundary curve whose curvature attains its algebraic maximum at a single point, and which could also be applied to a cylinder that has a closed boundary curve which is symmetric and whose curvature attains its algebraic maximum at two points. We decided to consider disturbances propagating along objects roughly corresponding to an elliptical bore, an elliptical rod, a wedge with a rounded tip, and a flat plane with a rounded ridge on it.

The exact forms of the chosen boundary curvature functions were suggested by the analytical form of the displacement function obtained in our high-frequency asymptotic results.[2] The high-frequency behavior of the disturbance can be determined in the vicinity of the cylinder

surface. As is shown in Appendix A, the disturbance corresponding to the zeroth-order mode, when evaluated at the surface of the cylinder, can be expressed as

$$\frac{c_T e^{i(\beta z-\omega t)}}{\omega b^{(0)}(0)}\mathbf{u}(\Xi,\eta)|_{\Xi=0}$$

$$= F(\eta)\exp\left[-(P\chi)^{1/2}G(\eta)\right]\left(\left[\frac{(b^2+a_T^2)}{2a_T}-a_L\right]\left[1+\frac{C(\eta)}{2(P\chi)^{1/2}}\right]\mathbf{n}\right.$$

$$\left.-\left[1-\frac{(b^2+a_T^2)}{2b^2}\right]\left\{\left(\frac{P}{\chi}\right)^{1/2}I(\eta)\mathbf{t}+ib\left[1+\frac{C(\eta)}{2(P\chi)^{1/2}}\right]\mathbf{k}\right\}\right). \quad (1)$$

Here $\mathbf{u}$ is the displacement, β is the propagation constant, z measures distance along the generators of the cylinder, ω is the frequency, and t is the time. A right-handed coordinate system is used, with unit vectors $\mathbf{n}$, $\mathbf{t}$, and $\mathbf{k}$ in the directions of the inward normal, tangent to the cross-sectional boundary curve, and along the generators of the cylinder, respectively. Here $\Xi = n/\ell$, where n represents distance from the surface along the inward normal and ℓ is a characteristic length; also $\eta = s/\ell$, where s is signed arc length along the boundary curve. The normalized unit of length, corresponding to the characteristic length ℓ, is depicted in Figs. 2, 3, and 4 for the particular cross-sectional boundary curves considered. The quantities b, a_T, a_L, and P are constants defined in Appendix A, and $b^{(0)}(0)$ is a normalization constant. We have

$$\chi = \omega\ell/c_T \gg 1, \quad (2)$$

where c_T is a constant representing the transverse wave velocity of the medium. Thus, the parameter χ is proportional to the frequency ω and is assumed to be large. The functions $C(\eta)$, $F(\eta)$, $G(\eta)$, and $I(\eta)$ all involve the curvature function $K(\eta) = \ell\kappa(s)$; as is shown in Appendix A, $C(\eta)$, $F(\eta)$, and $G(\eta)$ are defined as integrals of certain functions of the curvature function. It was to evaluate these integrals and the integral of the curvature function analytically that we chose the specific curvature functions.

The boundary curves are then given by the functions $X(\eta)$ and $Y(\eta)$ defined by[5]

$$\frac{dX}{d\eta} = \cos\int_0^\eta K(\zeta)d\zeta,$$

$$\frac{dY}{d\eta} = -\sin\int_0^\eta K(\zeta)d\zeta. \quad (3)$$

To describe an ellipse-like bore, we set

$$K_1(\eta) = -1 + 2k\cos 2\eta, \qquad 0 \leqq k \leqq \tfrac{1}{2}, \quad (4)$$

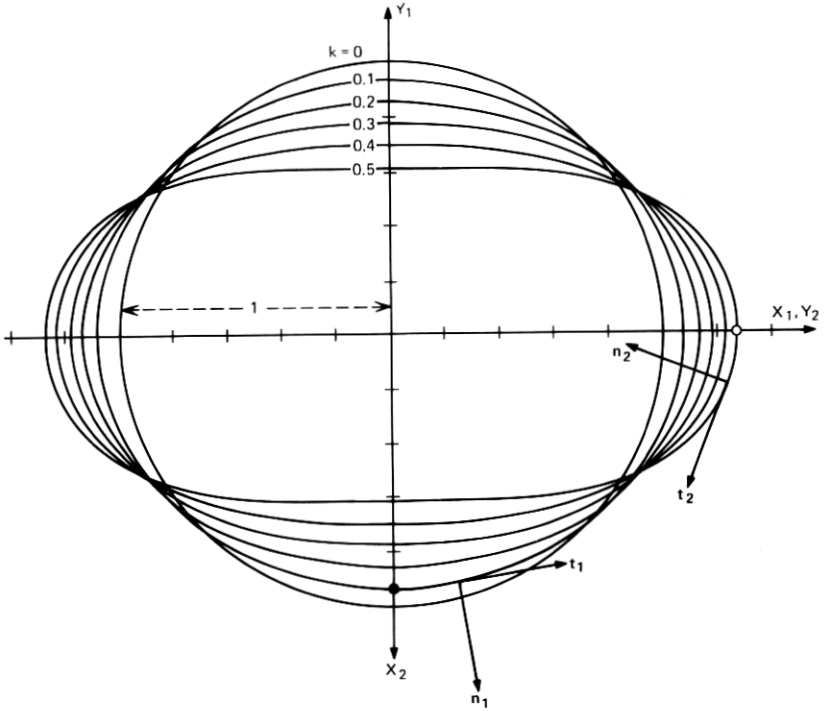

Fig. 2—Boundary curves corresponding to the ellipse-like bore and rod for various values of k.

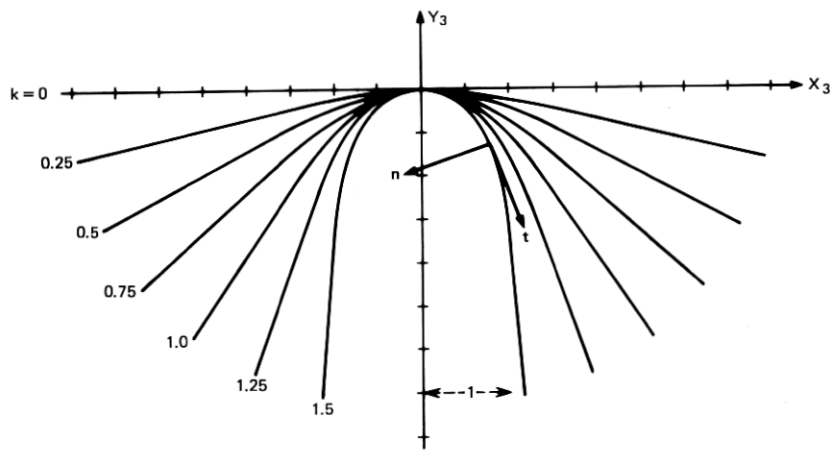

Fig. 3—Boundary curves corresponding to the rounded wedge for various values of k.

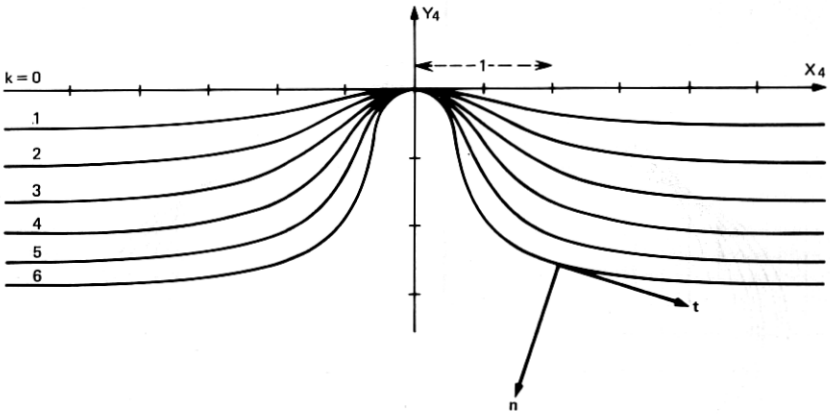

Fig. 4—Boundary curves corresponding to the ridged plane for various values of k.

while

$$K_2(\eta) = 1 + 2k \cos 2\eta, \qquad 0 \leqq k \leqq \tfrac{1}{2} \tag{5}$$

corresponds to an ellipse-like rod. Equations (4) and (5) actually describe the same boundary curve with circumference $2\pi\ell$. Notice that in both instances $\eta = 0$ corresponds to a point of maximum algebraic curvature. Also, the curvature is negative for the bore, because of our convention that $\mathbf{n}$ is directed into the region. The curvature function

$$K_3(\eta) = k \operatorname{sech}^2\eta, \qquad 0 \leqq k \leqq \pi/2 \tag{6}$$

corresponds to a wedge-like object similar to a hyperbolic cylinder. Finally,

$$K_4(\eta) = k[\epsilon^2 - \tanh^2\eta(\operatorname{sech}^2\eta + \epsilon)^2], \qquad \epsilon = \tfrac{1}{3}\left(1 + \sqrt{\frac{11}{5}}\right) \tag{7}$$

describes a rounded ridge on a plane. The value for ϵ is found from the condition $\int_0^\infty K(\eta)d\eta = 0$. As with the other cases, there is also a restriction on k. It is complicated so we do not write it here. In each case, k is a parameter that can be varied.

The boundary curves corresponding to the curvature functions in (4) to (7) were obtained numerically. In Fig. 2, we show the boundary curves corresponding to the ellipse-like bore and rod for various values of k. The unit of length is indicated in the figure. Notice that $k = 0$ corresponds to a circular bore or rod. The dot represents the point $\eta = 0$ for the bore corresponding to $k = 0.1$, indicating that the points of maximum curvature lie on the Y_1 axis. For the bore, the vectors $\mathbf{n}_1$ and $\mathbf{t}_1$ indicate the directions of the normal into the region and the tangent to the curve.

Similarly, the circle represents the point $\eta = 0$ for the rod corresponding to $k = 0.5$, indicating that the points of maximum curvature lie on the Y_2 axis. Note that the axes for the rod have been rotated by 90 degrees from those for the bore. For the rod, the vectors $\mathbf{n}_2$ and $\mathbf{t}_2$ indicate the directions of the inward normal and the tangent to the curve. In Figs. 3 and 4, we show the boundary curves for the rounded wedge and ridged plane, respectively, for various values of k. The unit of length is indicated, as are the unit vectors $\mathbf{n}$ and $\mathbf{t}$.

At high frequencies, the asymptotic result (1) does not hold in the transition region between the case of cross-sectional boundary curves of nonconstant (and not "almost" constant) curvature, for which the modes are localized, and the case of constant curvature, for which they are not localized. However, a refined surface-wave approximation equation, to be discussed in Section IV, does give results in this transition region.

III. ASYMPTOTIC RESULTS

In this section, we present high-frequency asymptotic results based on evaluation of (1) for the bore, rod, wedge, and plane with a ridge. In each case, the results are for the fundamental, or zeroth-order, mode. The bore and the rod have closed boundary curves which are symmetric, and for which the curvature attains its algebraic maximum at two points. For such cylinders, the expansion (1) corresponds to two modes, the zeroth-order symmetric one and the zeroth-order antisymmetric one, for which the values of the propagation constant β differ by only an exponentially small amount.[1,2] This expansion is about the point of maximum algebraic curvature at $\eta = 0$ and is valid for $|\eta| < \pi/2$. There is an analogous expansion about the point of maximum algebraic curvature at $\eta = \pi$ which is valid for $|\eta - \pi| < \pi/2$. Each expansion is not expected to be precise in regions where the disturbance is very small and the two modes differ. It is necessary to ensure that the disturbance is confined to regions near points of maximum algebraic curvature so that it is indeed small where the two modes are known to differ. From (1), (29), (33), and (35), this can be viewed as a requirement that the frequency parameter χ be sufficiently large and that the deviation of the curvature from a constant value not be small.

Equation (1), which is valid on the surface of the cylinder, was obtained from (39) in Appendix A, which holds also near the surface. In the derivation of the latter equation, it was necessary to assume that if the center of curvature for a point on the cross-sectional boundary curve lies *within* the region defining the cylinder, then the disturbance must be negligible at that point. This means that for the rod, wedge, and ridged plane, the results are applicable only if the frequency is high enough that the disturbance is confined close to the surface of the cylinder. Mathe-

matically, this means that each exponential term in (39) must be very small when evaluated at the value of Ξ corresponding to the minimum radius of curvature. These conditions result in an approximate lower bound on the frequency parameter χ, namely that

$$\chi \gtrsim 10\, K(0)/a_T. \tag{8}$$

The constant a_T depends upon the Poisson ratio σ. For values of σ between 0 and ½, it turns out that a_T ranges between 0.56 and 0.31, respectively. Most of our numerical results were obtained with $\sigma = 0.16974$, which was taken as the Poisson ratio for fused silica.[6] For this value of σ, we have $a_T = 0.47$.

As can be seen from (1), the **n** and **k** components of the displacement $u_n(0,\eta)$ and $u_k(0,\eta)$ each contain a factor $[1 + \frac{1}{2}C(\eta)(P\chi)^{-1/2}]$, whereas the **t** component $u_t(0,\eta)$ contains a factor $I(\eta)(P/\chi)^{1/2}$. Then, in the lowest-order asymptotic approximation, A.0 in Fig. 1, the **t** component of the displacement does not even appear. To this order, the solution is like that for Rayleigh waves traveling on the surface of a plane infinite half space except that it is multiplied by a factor that describes the confinement of the disturbance due to the cylinder curvature. In the next-order asymptotic approximation, A.1 in Fig. 1, the effect is to multiply this solution by an additional factor and to add a **t** component of displacement. Since it turns out computationally that u_t is a few percent of the size of u_n or u_k, we shall concentrate our attention on u_n and u_k. Since these two components are proportional to each other, it suffices to treat the quantities

$$S_0(\eta) = F(\eta)\exp[-(P\chi)^{1/2}G(\eta)], \tag{9}$$

$$S_1(\eta) = S_0(\eta)[1 + \tfrac{1}{2}C(\eta)(P\chi)^{-1/2}], \tag{10}$$

which are proportional to the **n** and **k** displacement components in the lowest-order and next-higher-order asymptotic approximations, A.0 and A.1, respectively, and which are normalized to unity at $\eta = 0$. We shall mostly discuss the more accurate approximation $S_1(\eta)$.

Figures 5 and 6 illustrate some results obtained for the ellipse-like bore whose cross-sectional curvature function is given by (4). Because of the symmetries of the boundary curve, it is only necessary to consider values of η between 0, which corresponds to a point of maximum algebraic curvature, and $\pi/2$, which corresponds to a point one quarter of the way around the curve. In both figures, we plot the first-order asymptotic approximation $S_1(\eta)$ from $\eta = 0$ to a value of η less than $\pi/2$ for which the disturbance is relatively small.

In Fig. 5, we show $S_1(\eta)$ for several values of the frequency parameter χ. The constant k in (4) was chosen to be 0.5; the Poisson ratio was chosen to be 0.16974, corresponding to fused silica.If we take the transverse wave

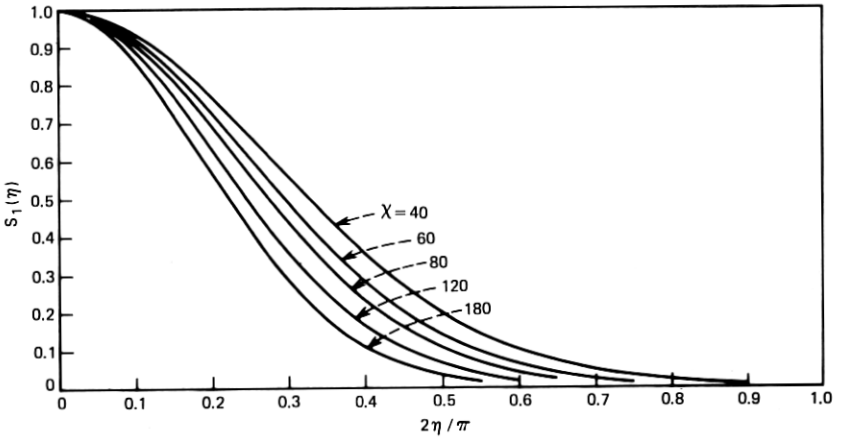

Fig. 5—First-order asymptotič approximation $S_1(\eta)$ for the bore, with $k = 0.5$, plotted as a function of η for various values of the frequency parameter χ and Poisson ratio $\sigma = 0.16974$.

velocity for fused silica to be 3764 m/s, then for $\ell = 3 \times 10^{-4}$ m the frequency corresponding to $\chi = 40$ is approximately 80 MHz. It is strikingly apparent that the disturbance is indeed confined to a region near the point of maximum algebraic curvature $\eta = 0$. There is, of course, similar confinement to the region near $\eta = \pi$. Such confinement near a point of maximum algebraic curvature shows up in a similar manner in the computations for rods, wedges, and ridges on planes. We also see that the confinement becomes even more pronounced as the frequency parameter χ increases.

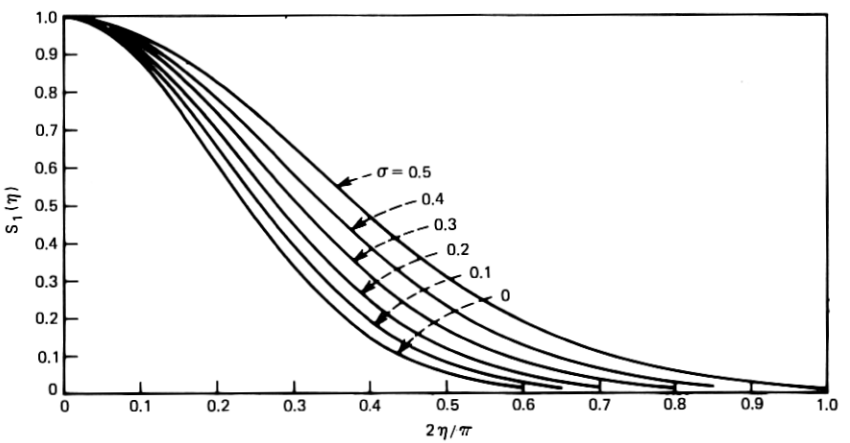

Fig. 6—First-order asymptotic approximation $S_1(\eta)$ for the bore, with $k = 0.5$, plotted as a function of η for frequency parameter $\chi = 80$ and various values of the Poisson ratio σ.

As the ellipse-like bore becomes more like a circular bore (k decreases), the confinement near points of maximum algebraic curvature decreases. This is to be expected since in the limiting case of a perfectly circular bore, there is no such confinement at all. We do not include a figure here to exhibit the way the confinement changes with k, as the effect will be vividly demonstrated later in Section IV where surface waves on "almost" circular bores are discussed.

In Fig. 6, we fix $\chi = 80$ and $k = 0.5$, and show $S_1(\eta)$ for various values of the Poisson ratio σ. The confinement increases as σ decreases.

These results are quite representative of all those we obtained for the bore, rod, wedge, and plane with a ridge. Other curves for $S_1(\eta)$ are qualitatively very similar. For example, in Fig. 7, we show $S_1(\eta)$ for a plane with a ridge on it. In this case, the curvature function is given by (7), with $k = 3$. We fixed $\sigma = 0.16974$ and varied the frequency parameter χ. Because other results are so similar, we do not show any specific curves for the rod or wedge.

We next compare the lowest-order asymptotic approximation $S_0(\eta)$ with the first-order asymptotic approximation $S_1(\eta)$. Here, some distinctions do arise in our computations for the various cylinders. In considering the ellipse-like bore, we find that for values of the parameters in the ranges previously discussed, the curves $S_0(\eta)$ are hardly distinguishable from the curves $S_1(\eta)$. This is not always the case for the rod, wedge, and ridge on a plane. To give an example for which the first-order correction term is significant, we show in Fig. 8 the functions $S_0(\eta)$ and $S_1(\eta)$ corresponding to a rounded wedge, with $\chi = 40$, $k = 1.0$, and $\sigma = 0.16974$. Similar results can be obtained for the rod and the plane with a ridge on it when the frequency parameter χ is in the lower part of the range being considered. In all cases, the first-order correction becomes noticeably smaller as χ is increased. We expect the second-order correction to be negligible.

The normalized phase and group velocities are

$$w_p = \frac{\omega}{\beta c_T}, \qquad w_g = \left(c_T \frac{d\beta}{d\omega}\right)^{-1}, \tag{11}$$

where c_T is the transverse-wave velocity. From the asymptotic results,[2] it is found that

$$w_p = \frac{1}{b} - \frac{d_0 P}{2b^3\chi} + \frac{(-d_2 P)^{1/2}}{2b^3\chi^{3/2}} + \frac{(d_0^2 P^2 - 2b^2 Q^2)}{4b^5\chi^2} + \ldots \tag{12}$$

and

$$w_g = \frac{1}{b} - \frac{(-d_2 P)^{1/2}}{4b^3\chi^{3/2}} + \frac{Q}{2b^3\chi^2} + \ldots, \tag{13}$$

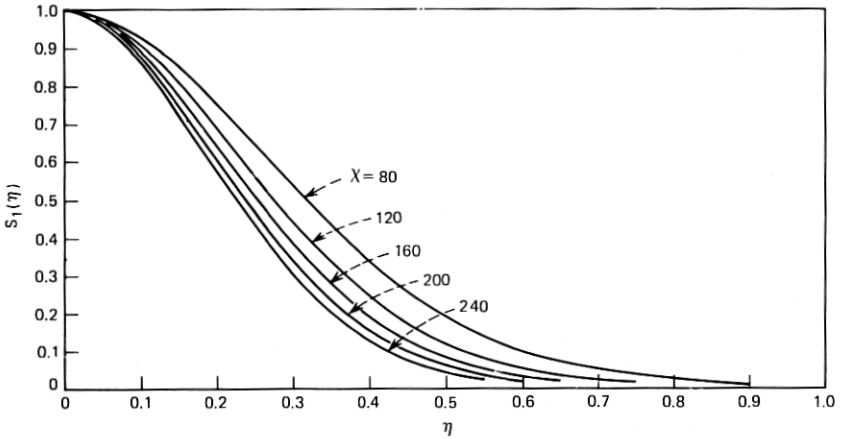

Fig. 7—First-order asymptotic approximation $S_1(\eta)$ for the ridged plane, with $k = 3$, plotted as a function of η for various values of the frequency parameter χ and Poisson ratio $\sigma = 0.16974$.

where the constants b, d_0, d_2, P, and Q are defined in Appendix A. In particular, $1/b = c_R/c_T = w_R$ is the normalized Rayleigh wave velocity, and w_R is the solution of equation (24) which satisfies $0 < w_R < 1$. Both the phase and the group velocity asymptotically approach the Rayleigh wave velocity and, consequently, we define the normalized differential phase and group velocities by

$$\delta_p = w_p - 1/b, \qquad \delta_g = w_g - 1/b. \tag{14}$$

The asymptotic approximations δ_{p1}, δ_{p2}, and δ_{p3} to δ_p are obtained by retaining terms through orders χ^{-1}, $\chi^{-3/2}$, and χ^{-2} respectively in the

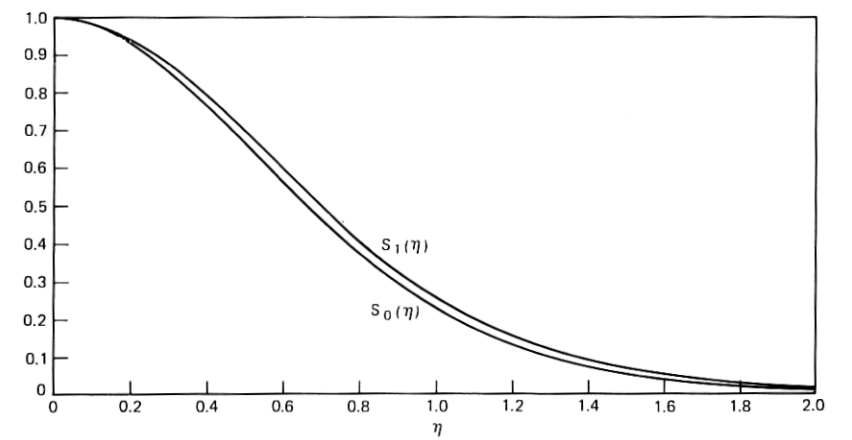

Fig. 8—Comparison of lowest- and first-order asymptotic approximations $S_0(\eta)$ and $S_1(\eta)$ for the rounded wedge, with $k = 1.0$, plotted as functions of η for frequency parameter $\chi = 40$ and Poisson ratio $\sigma = 0.16974$.

expansion (12). Similarly, the approximations δ_{g2} and δ_{g3} to δ_g are obtained by retaining terms through orders $\chi^{-3/2}$ and χ^{-2} respectively in the expansion (13).

In Fig. 9, we show the approximations δ_{p2} and δ_{p3} to the normalized differential phase velocity as a function of the frequency parameter χ for the ellipse-like bore, with $k = 0.5$ and $\sigma = 0.16974$. We do not plot δ_{p1}, as it can be shown to be identically equal to zero for this case. Notice that the convergence is quite good. This is also true for the approximations δ_{g2} and δ_{g3} to the normalized differential group velocity, which are shown in Fig. 10.

For cylinders of other cross-sectional shapes, the convergence is not always so good, particularly for the differential group velocities. In Tables I(a) and I(b), we show δ_{p1}, δ_{p2}, δ_{p3}, and δ_{g2}, δ_{g3}, respectively, for the bore, rod, wedge, and ridged plane; here $\chi = 80$, $\sigma = 0.16974$, and k varies. The convergence improves as χ increases.

In Figs. 11 and 12, we show one additional set of approximations to the differential phase and group velocities, respectively, as a function of χ. Here, the curves are for the wedge, with $k = 1.0$ and $\sigma = 0.16974$.

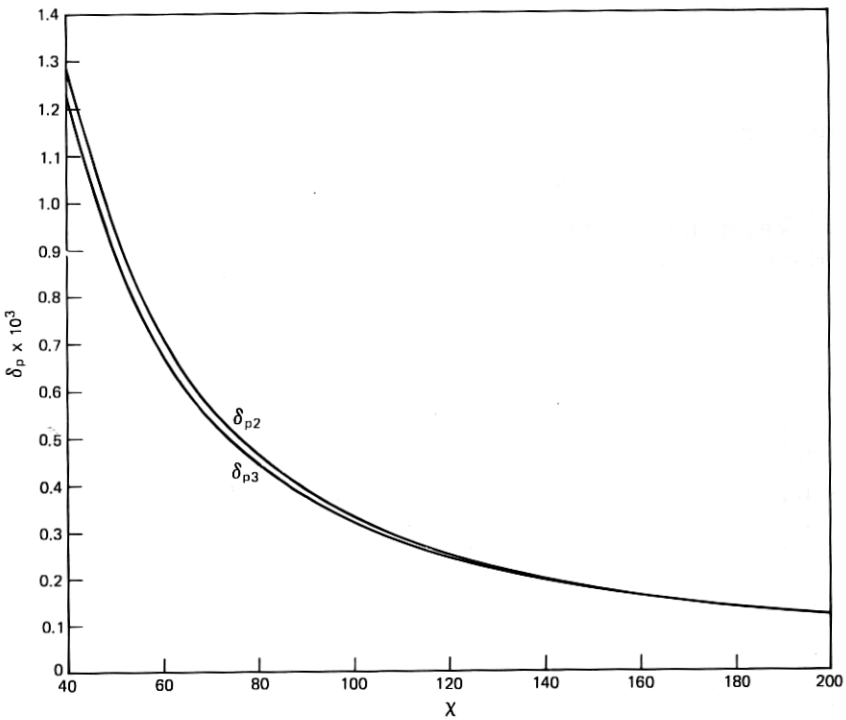

Fig. 9—Asymptotic approximations δ_{p2} and δ_{p3} to the normalized differential phase velocity as a function of the frequency parameter χ for the bore; $k = 0.5$ and Poisson ratio $\sigma = 0.16974$.

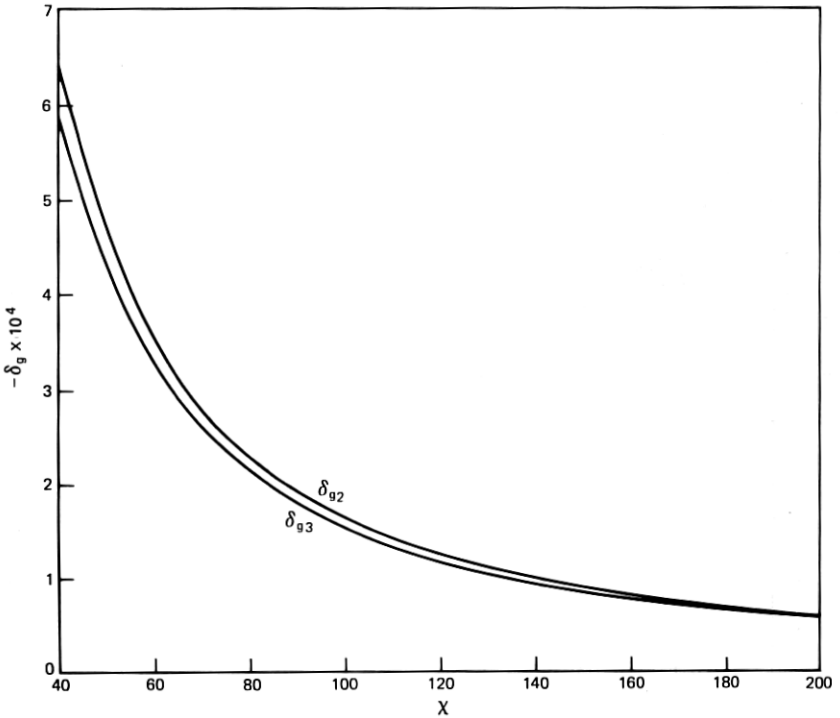

Fig. 10—Asymptotic approximations δ_{g2} and δ_{g3} to the normalized differential group velocity as a function of the frequency parameter χ for the bore; $k = 0.5$ and Poisson ratio $\sigma = 0.16974$.

IV. SURFACE-WAVE APPROXIMATIONS

In this section, we consider two related equations that describe the high-frequency behavior of the surface-wave modes. We call these equations the lowest-order approximate equation and the refined approximate equation. They are subject to the same restrictions about the disturbances being confined near the surface as are the asymptotic equations of Section III which describe the zeroth-order mode. The surface-wave approximations B.0 and B.1 (see Fig. 1) permit a more complete analysis of the higher-order modes. The refined approximation B.1 also describes the behavior of the modes in the transition region, at high frequencies, between the case of cross-sectional boundary curves of nonconstant (and not "almost" constant) curvature, for which the modes are localized, and the case of constant curvature, for which they are not localized.

In the refined surface-wave approximation[3] the displacement, when evaluated at the surface of the cylinder, can be expressed in the form

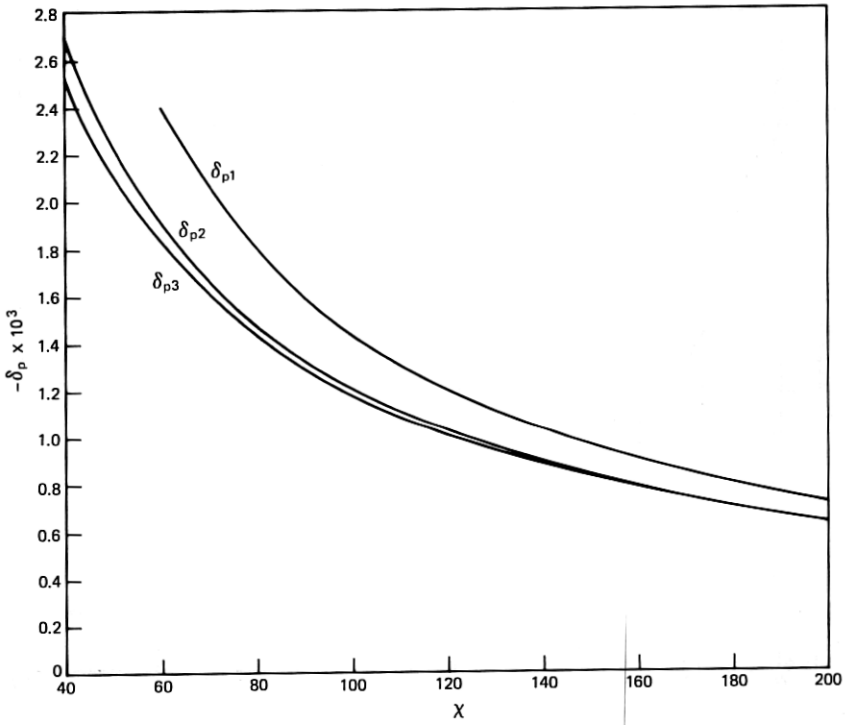

Fig. 11—Asymptotic approximations δ_{p1}, δ_{p2}, and δ_{p3} to the normalized differential phase velocity as a function of the frequency parameter χ for the wedge; $k = 1.0$ and Poisson ratio $\sigma = 0.16974$.

$$\frac{c_T}{\omega} e^{i(\beta z - \omega t)} \mathbf{u}|_{n=0} = \left[\frac{(b^2 + a_T^2)}{2a_T} - a_L\right] H\mathbf{n} + \left[1 - \frac{(b^2 + a_T^2)}{2b^2}\right] \left(\frac{1}{\chi}\frac{dH}{d\eta}\mathbf{t} - ibH\mathbf{k}\right), \quad (15)$$

where H satisfies the refined approximate equation

$$\frac{d^2H}{d\eta^2} + \{\chi[PK(\eta) - 2b\nu] - \nu^2 + \nu SK(\eta) - \tau[K(\eta)]^2\}H = 0. \quad (16)$$

Here the frequency parameter χ is as defined in (2), $K(\eta)$ is the curvature function, $\eta = s/\ell$ as before, and P, S, and τ are constants. The parameter ν is an eigenvalue, which is to be determined from a periodicity condition in the case of a closed boundary curve, and from an appropriate condition at infinity in the case of an open boundary curve. The propagation constant β is given by

$$\beta\ell = b\chi + \nu, \quad (17)$$

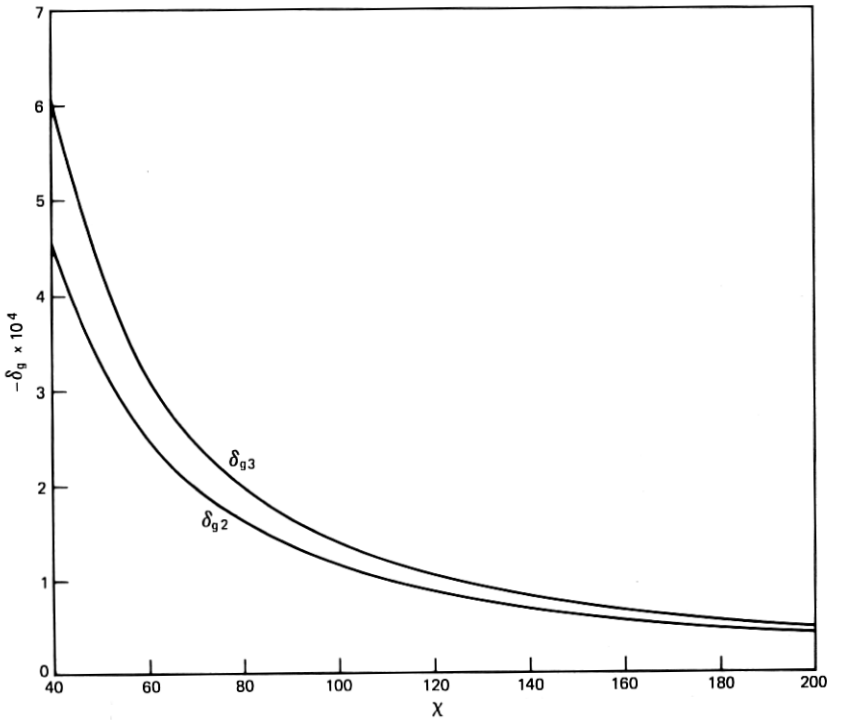

Fig. 12—Asymptotic approximations δ_{g2} and δ_{g3} to the normalized differential group velocity as a function of the frequency parameter χ for the wedge; $k = 1.0$ and Poisson ratio $\sigma = 0.16974$.

and the normalized phase and group velocities are

$$w_p = (b + \nu/\chi)^{-1}, \qquad w_g = (b + d\nu/d\chi)^{-1}. \tag{18}$$

In this refined approximation, correction terms[3] of order $1/\chi$ could be included in the **n** and **k** components of the surface displacement given by (15). However, for the numerical cases considered in this paper, it turns out that these corrections, which differ for the two components, are of at most a few percent, so we do not write out these terms here.

The lowest-order approximation B.0 (see Fig. 1) is obtained by omitting those terms multiplying H in (16) which are independent of χ. Having done this, we replace H by H_0 in (15) and ν by ν_0 in (17) and (18), where H_0 satisfies the lowest-order approximate equation

$$\frac{d^2H_0}{d\eta^2} + \chi[PK(\eta) - 2b\nu_0]H_0 = 0. \tag{19}$$

It was shown[3] that the asymptotic approximation (1) for the surface displacement of the zeroth-order mode may be derived from (15) and

Table I(a) — Asymptotic approximations to the normalized differential phase velocity of the zeroth-order mode for various cross-sectional shapes; frequency parameter $\chi = 80$ and Poisson ratio $\sigma = 0.16974$

Shape	k	$-\delta_{p1} \times 10^3$	$-\delta_{p2} \times 10^3$	$-\delta_{p3} \times 10^3$
Bore	0.3	−0.718	−1.072	−1.068
	0.4	−0.359	−0.767	−0.756
	0.5	0	−0.457	−0.442
Rod	0.1	2.15	1.95	1.86
	0.2	2.51	2.22	2.10
	0.3	2.87	2.52	2.35
	0.4	3.23	2.82	2.61
	0.5	3.59	3.13	2.87
Wedge	0.5	0.898	0.669	0.681
	1.0	1.80	1.47	1.43
	1.5	2.69	2.30	2.17
Ridged Plane	2	2.46	1.63	1.57
	3	3.69	2.67	2.45
	4	4.92	3.74	3.29
	5	6.15	4.83	4.09

Table I(b) — Asymptotic approximations to the normalized differential group velocity of the zeroth-order mode for various cross-sectional shapes; frequency parameter $\chi = 80$ and Poisson ratio $\sigma = 0.16974$

Shape	k	$-\delta_{g2} \times 10^4$	$-\delta_{g3} \times 10^4$
Bore	0.3	1.77	1.73
	0.4	2.04	1.92
	0.5	2.28	2.14
Rod	0.1	1.02	1.83
	0.2	1.44	2.60
	0.3	1.77	3.32
	0.4	2.04	4.04
	0.5	2.28	4.78
Wedge	0.5	1.14	1.02
	1.0	1.61	1.99
	1.5	1.98	3.18
Ridged Plane	2	4.17	4.65
	3	5.11	7.14
	4	5.90	10.10
	5	6.60	13.60

the refined approximate equation (16). Also, the lowest-order asymptotic approximation, in which the terms involving $C(\eta)[2(P\chi)^{1/2}]^{-1}$ do not appear in (1), may be derived from (19). However, in the transition region between the cases of nonconstant (and not "almost" constant) curvature and constant curvature, where the asymptotic results are not valid, eqs.

(16) and (19) have to be solved numerically, in general; it was shown,[3] though, that (19) may be solved analytically in the case of the curvature function $K_3(\eta)$ given by (6). We will see later how the results obtained from the numerical solution of (16) and (19) compare with the asymptotic results A.0 and A.1 (Fig. 1) in their common region of validity.

As we will see, the lowest-order approximate eq. (19) is generally not sufficiently accurate in the transition region, when the curvature is "almost" constant. An exception is the case of the curvature function $K_3(\eta)$ given by (6), the reason being that the curvature is small in this case, tending to zero as $k \to 0$, so that the terms involving S and τ in (16) are small.

4.1 Circular bore

We first consider the case of a circular bore of radius ℓ, with $K(\eta) \equiv -1$, corresponding to $k = 0$ in (4). We compare our results from the lowest-order and refined approximate equations with the exact theoretical results[4] for the fundamental mode in a circular bore.

For the lowest-order surface mode, with $K(\eta) \equiv -1$ in (16) and (19), both H_0 and H are constant, and the corresponding eigenvalues are

$$\nu_0 = -\frac{P}{2b}, \qquad \nu = -\left(b\chi + \frac{S}{2}\right) \pm \left[\left(b\chi + \frac{S}{2}\right)^2 - (P\chi + \tau)\right]^{1/2}. \tag{20}$$

Note that $d\nu_0/d\chi = 0$, so that in the lowest-order approximation, from (18), the group velocity is equal to the Rayleigh wave velocity.

The exact theoretical dispersion relation for the fundamental mode in a circular bore was solved numerically for the normalized phase velocity w_p by Rosenberg, Schmidt, and Coldren[6] for Poisson ratio $\sigma = 0.16974$, corresponding to fused silica. They also calculated the corresponding value of the normalized group velocity w_g. In Table II(a), we compare their values of w_p as a function of the frequency parameter χ with those calculated from (18) and (20). We add the subscripts L and R to w_p to denote the lowest-order and refined approximate values of the phase velocity, respectively. Similarly, in Table II(b), we compare the exact theoretical and refined approximate values of w_g. The normalized value of the Rayleigh wave velocity is $1/b = 0.905727$.

Notice that the lowest-order surface-wave approximation w_{pL} is reasonably close to w_p and that the refined surface-wave approximations w_{pR} and w_{gR} are remarkably close to w_p and w_g, respectively. The agreement improves as the frequency parameter χ increases.

Rosenberg, Schmidt, and Coldren[6] plotted normalized differential phase and group velocities versus χ. In Fig. 13, for purposes of comparison, the normalized quantities $(bw - 1)/(b - 1)$ are plotted against χ for $w = w_{pL}, w_{pR}, w_p, w_{gR}$, and w_g. The dots are for values corresponding

Table II(a) — Comparison of lowest-order and refined approximate and exact theoretical values of the normalized phase velocity of the fundamental mode in a circular bore; frequency parameter χ has various values and Poisson ratio $\sigma = 0.16974$

χ	w_{pL}	w_{pR}	w_p
6	0.930315	0.938221	0.937969
8	0.924044	0.928858	0.928829
10	0.920321	0.923570	0.923583
12	0.917856	0.920199	0.920219
14	0.916104	0.917874	0.917893
16	0.914794	0.916179	0.916195
18	0.913777	0.914892	0.914905
20	0.912966	0.913882	0.913893
22	0.912303	0.913069	0.913078

Table II(b) — Comparison of refined approximate and exact theoretical values of the normalized group velocity of the fundamental mode in a circular bore; frequency parameter χ has various values and Poisson ratio $\sigma = 0.16974$

χ	w_{gR}	w_g
6	0.901046	0.902112
8	0.902532	0.902825
10	0.903408	0.903522
12	0.903968	0.903962
14	0.904347	0.904390
16	0.904615	0.904644
18	0.904812	0.904873
20	0.904961	0.904967
22	0.905077	0.905134

to w_p and w_g. Note that the normalized values of w_g do not lie precisely on a smooth curve. The values of w_g were obtained through numerical differentiation once the values of w_p had been calculated from the exact theoretical dispersion relation.[6] We suspect that the discrepancy is due to numerical difficulties in their computations.

4.2 Ellipse-like bore and rod

We now consider the ellipse-like bore and rod corresponding to the curvature functions $K_1(\eta)$ and $K_2(\eta)$ given by (4) and (5). The eigenvalue problems for the refined and lowest-order approximate equations (16) and (19) were solved numerically. It suffices to consider the interval $0 \leqq \eta \leqq \pi/2$, because the modes are either symmetric or antisymmetric about $\eta = 0$, and about $\eta = \pi/2$, so that $H'(0) = 0$ or $H(0) = 0$, and $H'(\pi/2) = 0$ or $H(\pi/2) = 0$.

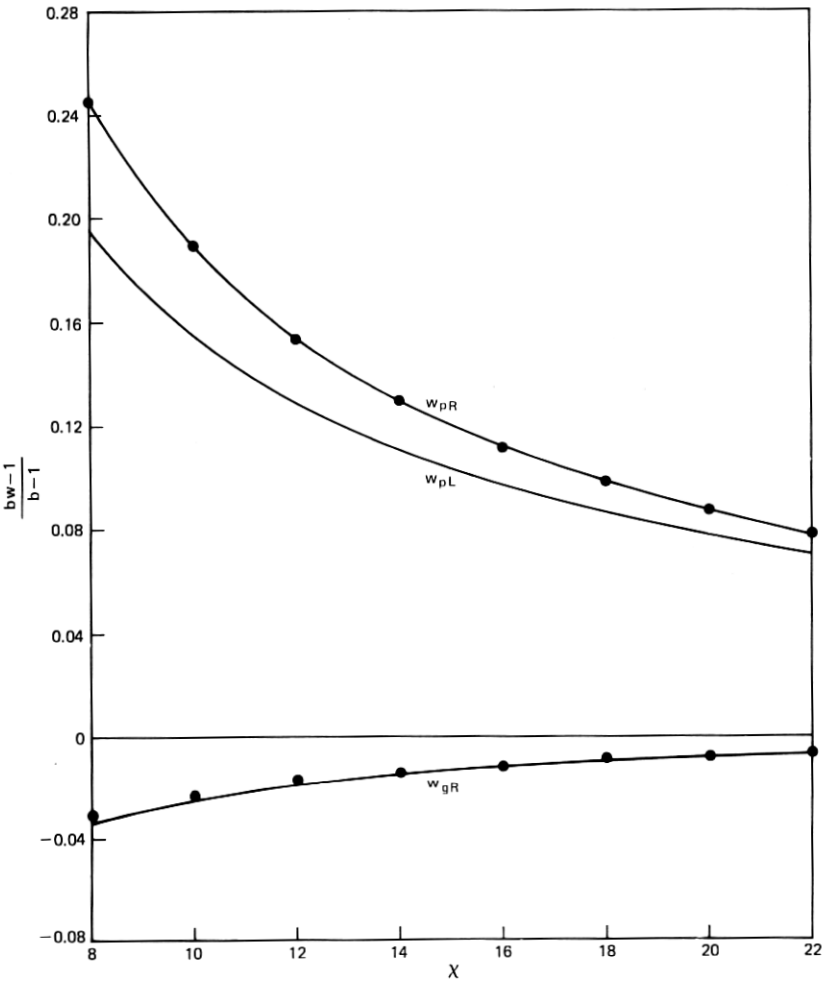

Fig. 13—Normalized differential phase and group velocities $(bw - 1)/(b - 1)$ as a function of the frequency parameter χ for the circular bore, with Poisson ratio $\sigma = 0.16974$. The curves correspond to the surface-wave approximations w_{pL}, w_{pR}, and w_{gR} and the dots correspond to the exact theoretical results w_p and w_g.

A "shooting" method was used, which involves making an initial guess for the eigenvalue ν, and numerically integrating the differential equation for $H(\eta)$ from $\eta = \pi/2$ to $\eta = 0$. The value of ν was adjusted iteratively, in the manner described in Appendix B, until the boundary condition at $\eta = 0$ was satisfied with sufficient accuracy. The initial iterations were done in single precision, and the final ones in double precision, and only a few iterations were required to obtain the desired accuracy. The numerical integrations were done from $\eta = \pi/2$ to $\eta = 0$, since in the asymptotic region the mode decays exponentially away from $\eta = 0$, and

integration from $\eta = 0$ toward $\eta = \pi/2$ would lead to numerical instabilities in this case.

To calculate both the phase and group velocities from (18), it is necessary to know the values of both ν and $d\nu/d\chi$. Once the eigenvalue ν, and the corresponding eigenfunction $H(\eta)$ had been obtained, the value of $d\nu/d\chi$ was obtained by quadratures, using the expression (46) derived in Appendix B. The analogous expression for $d\nu_0/d\chi$ is given by (47).

4.2.1 Rod

We first compare the results of the numerical solution of (16) and (19) for the rod [$k = 0.3$ in (5)] with the asymptotic results A.0 and A.1 for $\chi = 40$. Here, and subsequently, the value of Poisson's ratio is taken to be $\sigma = 0.16974$. In Fig. 14, we plot the refined and lowest-order surface-wave approximations $H(\eta)$ and $H_0(\eta)$ for the zeroth-order symmetric mode, normalized to unity at $\eta = 0$. The dots and circles correspond to the first and lowest-order asymptotic approximations $S_1(\eta)$ and $S_0(\eta)$, respectively, as defined in (10) and (9). It is seen that the asymptotic approximations agree quite well with the numerical solution, except, as expected, near $\eta = \pi/2$. As the value of χ increases, the agreement becomes better near $\eta = \pi/2$, since the disturbance becomes exponentially small there.

When the value of $S_1(\eta)$ is sufficiently small near $\eta = \pi/2$, the zeroth-order mode which is antisymmetric about $\eta = \pi/2$, as well as that mode which is symmetric about $\eta = \pi/2$, is approximated by $S_1(\eta)$, as was argued in an earlier paper.[2] In Fig. 15, we plot $H(\eta)$ for the lowest-order symmetric and antisymmetric modes. The dots, as before, corre-

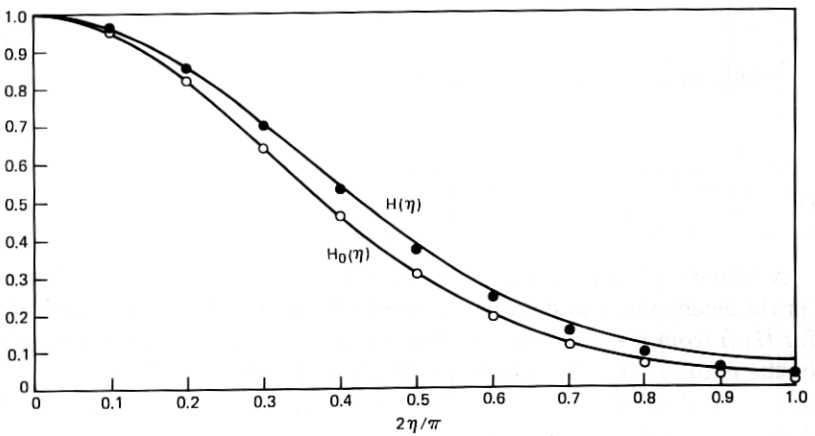

Fig. 14—Comparison of refined and lowest-order surface-wave approximations $H(\eta)$ and $H_0(\eta)$ for the zeroth-order symmetric mode, and corresponding asymptotic approximations $S_1(\eta)$ (dots) and $S_0(\eta)$ (circles) for the rod; $k = 0.3$, frequency parameter $\chi = 40$, and Poisson ratio $\sigma = 0.16974$.

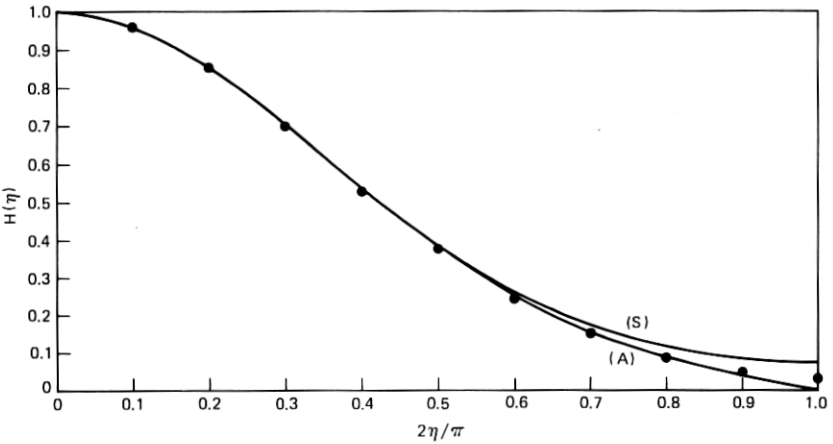

Fig. 15—Comparison of the refined surface-wave approximation $H(\eta)$ for the lowest-order symmetric (S) and antisymmetric (A) modes, and the first-order asymptotic approximation $S_1(\eta)$ (dots), for the rod; $k = 0.3$, frequency parameter $\chi = 40$, and Poisson ratio $\sigma = 0.16974$.

spond to the values of $S_1(\eta)$. To complete the comparison, in Table III we compare the asymptotic values of the differential phase and group velocities with the values obtained from (18).

Trends to notice are that the asymptotic approximations δ_{p2} and δ_{g2} to the differential phase and group velocities agree roughly with the lowest-order surface-wave approximations δ_{pL} and δ_{gL}. The correspondence between the next-order asymptotic approximations δ_{p3} and δ_{g3} and the refined surface-wave approximations δ_{pR} and δ_{gR} is somewhat better. The agreement is better for the differential phase velocities than it is for the differential group velocities. In all cases, the agreement improves as the frequency parameter χ increases.

As before, the **t** component of the displacement turns out to be a few percent of the **n** and **k** components of displacement.

Higher-order modes may be investigated also by solving the eigenvalue problem (16) numerically.

4.2.2 Bore

The agreement between the asymptotic and the numerical results is even better for the bore. We have already discussed the circular bore and we now consider the transition from this to a noncircular bore for which the asymptotic results are good, by letting k vary from 0 to ½ in (4). The results of the numerical solution of the refined and lowest-order approximate equations (16) and (19) for $\chi = 40$ and $\sigma = 0.16974$ are depicted in Figs. 16 and 17 for the lowest-order symmetric and antisymmetric modes, respectively. The full curves give the values of $H(\eta)$ (re-

Table III — Comparison of asymptotic and approximate values of the normalized differential phase and group velocities of the lowest-order symmetric (S) and antisymmetric (A) modes for the rod; $k = 0.3$, frequency parameter χ has various values, and Poisson ratio $\sigma = 0.16974$

	χ		
$-\delta_p \times 10^3$	40	60	80
δ_{p1}	5.745	3.830	2.873
δ_{p2}	4.745	3.286	2.519
δ_{pL} (S)	4.783	3.3010	2.5271
(A)	4.780	3.3007	2.5271
δ_{p3}	4.089	2.9942	2.3550
δ_{pR} (S)	4.075	2.9925	2.3555
(A)	4.066	2.9919	2.3554
$-\delta_g \times 10^3$	40	60	80
δ_{g2}	0.500	0.2722	0.1768
δ_{gL} (S)	0.428	0.2433	0.1611
(A)	0.442	0.2448	0.1613
δ_{g3}	1.120	0.5475	0.3317
δ_{gR} (S)	1.188	0.5693	0.3401
(A)	1.231	0.5730	0.3406

fined approximation) and the broken curves the values of $H_0(\eta)$ (lowest-order approximation); both curves are normalized to unity at $\eta = 0$ for the specified values of k.

For the symmetric mode, Fig. 16, $H_0(\eta) \equiv 1$ and $H(\eta) \equiv 1$ for $k = 0$, which agrees with the exact result for the circular bore. As k increases, the values of $H_0(\pi/2)$ and $H(\pi/2)$ decrease, becoming exponentially small for $k = 0.5$. It is seen that there is a significant difference between $H_0(\eta)$ and $H(\eta)$ for intermediate values of k. The lowest- and first-order asymptotic results agree very well with the numerical results obtained from (19) and (16) for $k = 0.5$. In Table IV we compare the lowest-order and refined approximations to the normalized differential phase and group velocities. We see that δ_{pL} and δ_{pR} differ by only a few percent; the agreement improves as k increases. The lowest-order approximation δ_{gL} for the normalized differential group velocity, however, is not very good, especially for the smaller values of k.

For the antisymmetric mode, Fig. 17, $H_0(\eta) = \cos \eta = H(\eta)$ for $k = 0$, which agrees with the exact result for the circular bore. The differences between $H_0(\eta)$ and $H(\eta)$, for intermediate values of k, are not as large as they are for the symmetric mode. It is noted that for $k = 0.5$, the curves of $H_0(\eta)$ and $H(\eta)$ are barely distinguishable from the corresponding ones

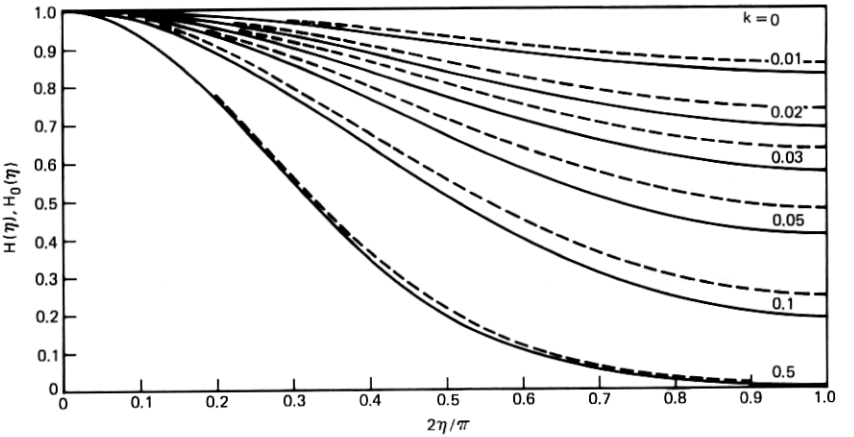

Fig. 16—Refined and lowest-order surface-wave approximations $H(\eta)$ (full curves) and $H_0(\eta)$ (broken curves) for the lowest-order symmetric mode for the bore; k has various values, frequency parameter $\chi = 40$, and Poisson ratio $\sigma = 0.16974$.

for the symmetric mode, as expected from the asymptotic results. The most significant difference is that $H_0(\pi/2) = 0 = H(\pi/2)$ for the antisymmetric mode, whereas $H_0'(\pi/2) = 0 = H'(\pi/2)$ for the symmetric mode. In Table V, we compare the lowest-order and refined approximations to the normalized differential phase and group velocities. As was the case for the symmetric mode, δ_{pL} and δ_{pR} differ by a few percent and the agreement generally improves as k increases. The lowest-order approximation δ_{gL} for the normalized differential group velocity, although not very good quantitatively, is qualitatively better than for the symmetric mode.

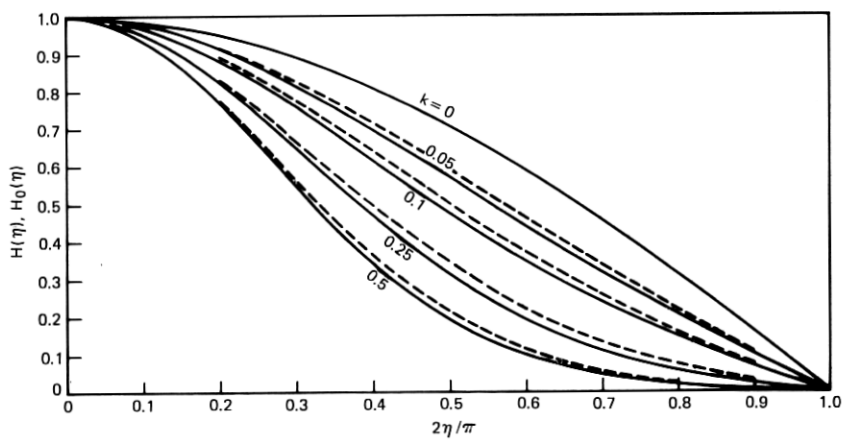

Fig. 17—Refined and lowest-order surface-wave approximations $H(\eta)$ (full curves) and $H_0(\eta)$ (broken curves) for the lowest-order antisymmetric mode for the bore; k has various values, frequency parameter $\chi = 40$, and Poisson ratio $\sigma = 0.16974$.

Table IV — Comparison of lowest-order and refined approximations to the normalized differential phase and group velocities of the lowest-order symmetric mode for the bore; k has various values, frequency parameter $\chi = 40$, and Poisson ratio $\sigma = 0.16974$

k	δ_{pL}	δ_{pR}	δ_{gL}	δ_{gR}
0	0.003605	0.003850	0	-0.224×10^{-3}
0.01	0.003602	0.003847	-0.275×10^{-5}	-0.226×10^{-3}
0.02	0.003594	0.003835	-0.108×10^{-4}	-0.234×10^{-3}
0.03	0.003580	0.003817	-0.234×10^{-4}	-0.247×10^{-3}
0.04	0.003562	0.003793	-0.396×10^{-4}	-0.262×10^{-3}
0.05	0.003539	0.003764	-0.583×10^{-4}	-0.279×10^{-3}
0.1	0.003374	0.003560	-0.162×10^{-3}	-0.358×10^{-3}
0.5	0.001232	0.001262	-0.581×10^{-3}	-0.636×10^{-3}

Table V — Comparison of lowest-order and refined approximations to the normalized differential phase and group velocities of the lowest-order antisymmetric mode for the bore; k has various values, frequency parameter $\chi = 40$, and Poisson ratio $\sigma = 0.16974$

k	δ_{pL}	δ_{pR}	δ_{gL}	δ_{gR}
0	0.003839	0.004066	-0.232×10^{-3}	-0.420×10^{-3}
0.01	0.003802	0.004024	-0.233×10^{-3}	-0.417×10^{-3}
0.02	0.003764	0.003981	-0.235×10^{-3}	-0.415×10^{-3}
0.03	0.003725	0.003936	-0.238×10^{-3}	-0.414×10^{-3}
0.04	0.003684	0.003890	-0.242×10^{-3}	-0.415×10^{-3}
0.05	0.003642	0.003842	-0.246×10^{-3}	-0.416×10^{-3}
0.1	0.003419	0.003590	-0.279×10^{-3}	-0.430×10^{-3}
0.5	0.001232	0.001262	-0.583×10^{-3}	-0.637×10^{-3}

4.3 Wedge

We now turn our attention to the wedge with a rounded tip, corresponding to the curvature function $K_3(\eta)$ given by (6). In this case, the lowest-order approximate equation (19) may be solved analytically.[3,7] The eigenfunctions are

$$H_0(\eta) \propto (sech\ \eta)^{a_m} F[2a_m + m + 1, -m; a_m + 1; \tfrac{1}{2}(1 - \tanh \eta)], \quad (21)$$

where

$$a_m = (P\chi k + \tfrac{1}{4})^{1/2} - m - \tfrac{1}{2} > 0, m = 0, \cdots, M, \quad (22)$$

and the corresponding eigenfunctions are given by

$$\nu_0 = a_m^2/(2b\chi). \quad (23)$$

The hypergeometric function[8] in (21) terminates, and is a polynomial of degree m in its argument. There is a finite number of modes, because of the requirement that $a_m > 0$, which ensures that $H_0(\eta) \to 0$ as $|\eta| \to \infty$. The even-order modes are symmetric about $\eta = 0$, and the odd-order modes are antisymmetric, so it suffices to consider $\eta \geqq 0$.

According to (22), the zeroth-order mode, corresponding to $m = 0$, always exists for $k > 0$. For $m = 0$, the hypergeometric function in (21) is identically equal to 1. If $P\chi k < 2$, in this approximation, then only the zeroth-order mode exists. In the limiting case, $k \to 0$, corresponding to a planar boundary; $a_0 \to 0$ and $H_0 \to 1$, for fixed η. That is, the zeroth-order mode tends to a Rayleigh wave on a plane infinite half space as $k \to 0$.

The eigenvalue problem for the refined approximate equation (16), with $K(\eta)$ given by (6), was solved numerically by a shooting method after a transformation of the independent variable had been made to reduce the interval of integration to a finite one. The details are given in Appendix C. For the symmetric modes, $H'(0) = 0$, and for the antisymmetric modes, $H(0) = 0$. Once the eigenvalue ν, and the corresponding eigenfunction $H(\eta)$ had been obtained, the value of $d\nu/d\chi$ was obtained by quadratures, using the expression (53) derived in Appendix C. The values of ν and $d\nu/d\chi$ were used in (18) to obtain the normalized phase and group velocities.

In Fig. 18, we plot the refined and lowest-order surface-wave approximations $H(\eta)$ and $H_0(\eta)$, normalized to unity at $\eta = 0$, for the zeroth-order mode for the wedge for $k = 1$, $\chi = 40$, and $\sigma = 0.16974$. We also make a comparison with the asymptotic results, A.0 and A.1 (Fig.

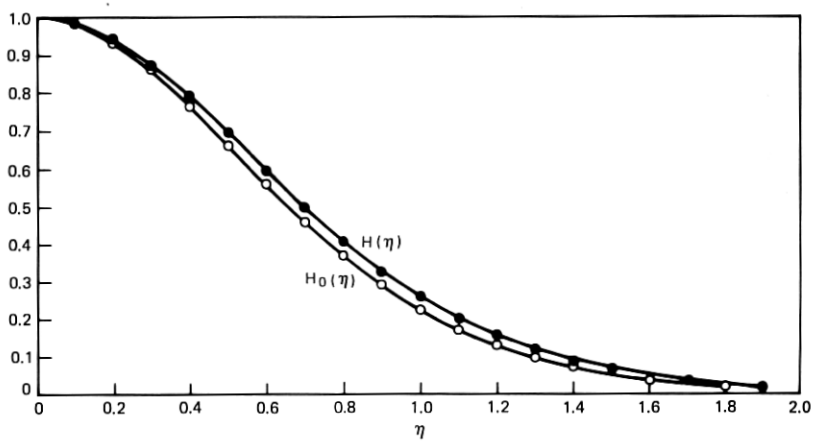

Fig. 18—Comparison of refined and lowest-order surface-wave approximations $H(\eta)$ and $H_0(\eta)$ for the zeroth-order mode, and corresponding asymptotic approximations $S_1(\eta)$ (dots) and $S_0(\eta)$ (circles) for the wedge; $k = 1.0$, frequency parameter $\chi = 40$, and Poisson ratio $\sigma = 0.16974$.

1), the dots and circles corresponding to the first- and lowest-order asymptotic approximations $S_1(\eta)$ and $S_0(\eta)$, respectively, as defined by (10) and (9). In Table VI, we compare the asymptotic values of the differential phase and group velocities with the values obtained from (18). The trends are similar to those we have noticed for the other cases. The asymptotic approximations δ_{p2} and δ_{g2} agree roughly with the lowest-order surface-wave approximations δ_{pL} and δ_{gL}. The higher-order asymptotic approximations δ_{p3} and δ_{g3} agree better with the refined surface-wave approximations δ_{pR} and δ_{gR}. The convergence is better for the differential phase velocities than it is for the differential group velocities; also, the agreement between the asymptotic and the surface-wave approximations is better.

In Figs. 19 and 20 we plot $H(\eta)$ and $H_0(\eta)$ for the remaining three modes. The odd-order, antisymmetric modes are normalized so that $H'(0) = 1$ and $H_0'(0) = 1$. In Table VII, we compare the corresponding values of the differential phase and group velocities.

Finally, we consider the transition region, between the case of non-constant (and not "almost" constant) curvature and constant curvature for the wedge, with $\chi = 40$ and $\sigma = 0.16974$. In Fig. 21, we plot $H(\eta)$ for the zeroth-order mode for several values of k between 0.01 and 1. We have not plotted $H_0(\eta)$ in this figure, since we compared $H_0(\eta)$ with $H(\eta)$ in Fig. 18 for $k = 1$ and found differences to be quite small for the smaller values of k. This is because the curvature is small when k is small, tending to zero as $k \to 0$, so that the terms involving S and τ in (16) are small. In Table VIII, we compare the lowest and refined approximations to the differential phase and group velocities as obtained from (18). In the transition region the agreement is good, both for the differential phase velocity and for the differential group velocity. As k increases and the lowest-order approximate equation becomes less accurate, discrepancies appear.

Table VI — Comparison of asymptotic and approximate values of the normalized differential phase and group velocities of the zeroth-order mode for the wedge; $k = 1.0$, frequency parameter $\chi = 40$, and Poisson ratio $\sigma = 0.16974$

$-\delta_p \times 10^3$	$\chi = 40$	$-\delta_g \times 10^3$	$\chi = 40$
δ_{p1}	3.591	—	—
δ_{p2}	2.678	δ_{g2}	0.457
δ_{pL}	2.778	δ_{gL}	0.351
δ_{p3}	2.515	δ_{g3}	0.605
δ_{pR}	2.521	δ_{gR}	0.614

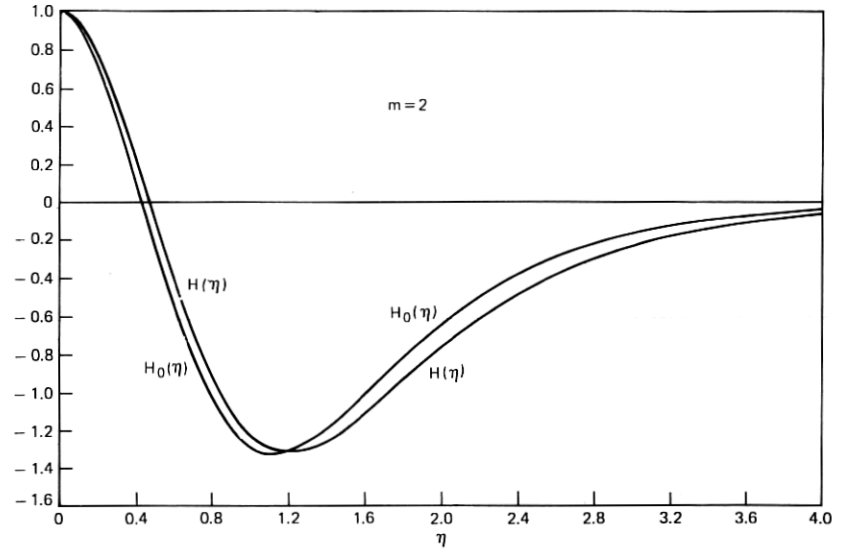

Fig. 19—Refined and lowest-order surface-wave approximations $H(\eta)$ and $H_0(\eta)$ for the second-order mode for the wedge; $k = 1.0$, frequency parameter $\chi = 40$, and Poisson ratio $\sigma = 0.16974$.

V. SUMMARY

We made numerical computations to learn about the propagation of elastic surface waves along cylindrical objects roughly corresponding to an elliptical bore, an elliptical rod, a wedge with a rounded tip, and a flat plane with a rounded ridge. The cross-sectional curvature functions describing these objects are given by eqs. (4) to (7). In earlier papers,[2,3] we had derived two approximate analytical descriptions of the surface-wave behavior: a high-frequency asymptotic approximation A, and one that we termed a surface-wave approximation B, as depicted in Fig. 1. Each of these approximations, in turn, was available in two forms: a lowest-order one and a higher-order or refined one. Here, we evaluated these approximations numerically.

We first performed a high-frequency asymptotic analysis of the disturbance in the vicinity of the cylinder surface and obtained the lowest-order, A.0, and next-higher-order, A.1, asymptotic approximations.[2] We used these approximations in the form shown in eq. (1), which describes the zeroth-order mode at the surface of the cylinder. For the bore and the rod, this equation corresponds to both the zeroth-order symmetric and antisymmetric modes. We also used the high-frequency asymptotic approximations to the phase and group velocities given by (12) and (13). The analysis involved two restrictions: the frequency had to be high enough that the disturbance was confined close to the surface

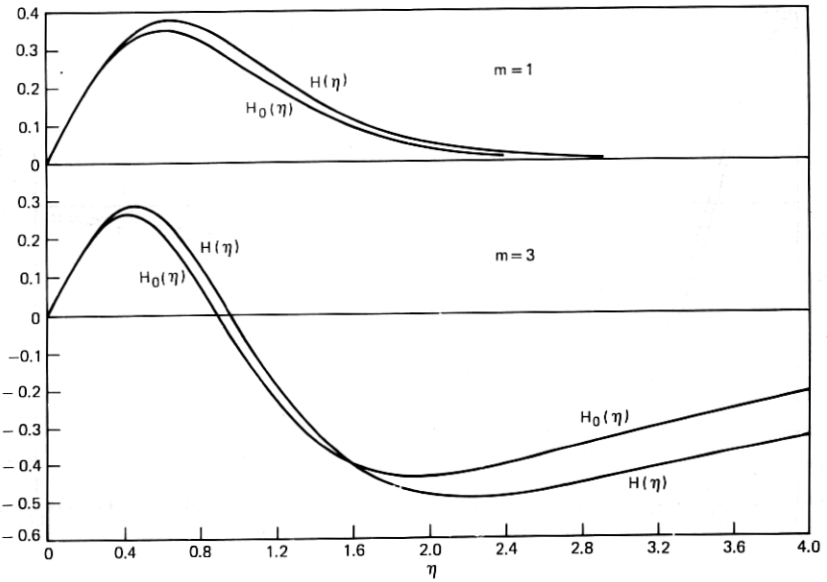

Fig. 20—Refined and lowest-order surface-wave approximations $H(\eta)$ and $H_0(\eta)$ for the first- and third-order modes for the wedge; $k = 1.0$, frequency parameter $\chi = 40$, and Poisson ratio $\sigma = 0.16974$.

of the cylinder, and the deviation of the cross-sectional curvature from a constant value had to be sufficiently large that the disturbance was confined near points of maximum algebraic curvature.

We also were able to describe the mode behavior at the cylinder surface[3] by the lowest-order, B.0, and refined, B.1, surface wave approximations (16) and (19). The phase and group velocities were given by (18). These surface-wave approximations B were subject to the same frequency restriction as were the asymptotic approximations A. In fact, the lowest-order and next-highest-order asymptotic approximations A.0 and A.1 for the zeroth-order mode could be obtained from the lowest-order and refined surface-wave approximations B.0 and B.1, respectively,

Table VII — Comparison of the lowest-order and refined approximations to the normalized differential phase and group velocities of the four modes for the wedge; $k = 1.0$, frequency parameter $\chi = 40$, and Poisson ratio $\sigma = 0.16974$

m	$-\delta_{pL} \times 10^3$	$-\delta_{pR} \times 10^3$	$-\delta_{gL} \times 10^3$	$-\delta_{gR} \times 10^3$
0	2.778	2.521	0.351	0.614
1	1.408	1.231	0.821	0.944
2	0.497	0.394	0.828	0.836
3	0.050	0.021	0.370	0.264

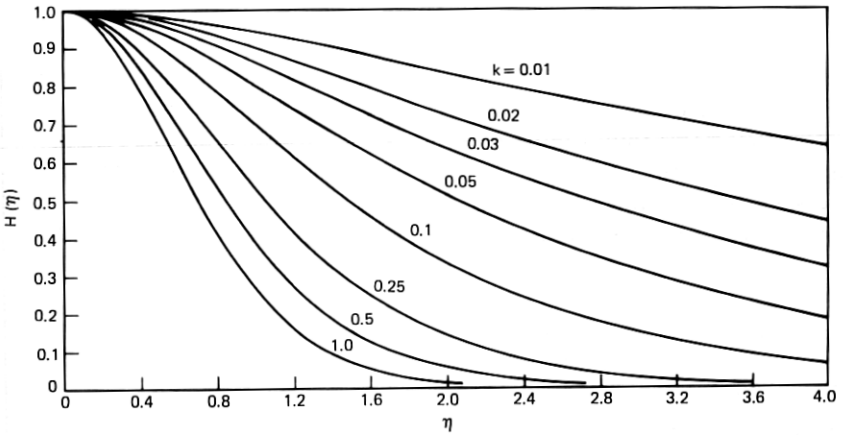

Fig. 21—Refined surface-wave approximation $H(\eta)$ for the zeroth-order mode for the wedge; various values of k, frequency parameter $\chi = 40$, and Poisson ratio $\sigma = 0.16974$.

provided that the above restriction on the cross-sectional curvature was satisfied.

The advantage of the surface-wave analysis B was that the curvature restriction could be dropped. It was possible, with the refined surface-wave approximation B.1 to describe the mode behavior, at high frequencies, in the transition region between the case of cross-sectional boundary curves of nonconstant (and not "almost" constant) curvature, for which the modes are localized, and the case of constant curvature, for which they are not localized. Also, the surface-wave approximations B permitted a more complete analysis of the higher-order modes. A disadvantage of the surface-wave approximations B was that they con-

Table VIII — Comparison of lowest-order and refined approximations to the normalized differential phase and group velocities of the zeroth-order mode for the wedge; k has various values, frequency parameter $\chi = 40$, and Poisson ratio $\sigma = 0.16974$

k	$-\delta_{pL} \times 10^3$	$-\delta_{pR} \times 10^3$	$-\delta_{gL} \times 10^4$	$-\delta_{gR} \times 10^4$
0.01	0.04302	0.04294	0.03381	0.03384
0.02	0.1426	0.1422	0.09537	0.09561
0.03	0.2763	0.2750	0.1635	0.1643
0.04	0.4333	0.4308	0.2324	0.2341
0.05	0.6076	0.6034	0.3003	0.3033
0.1	0.1639	0.1620	0.6116	0.6278
0.25	0.5424	0.5284	1.337	1.466
0.5	1.254	1.194	2.221	2.801
1.0	2.778	2.521	3.513	6.137

sisted of eigenvalue equations which, in general, had to be solved numerically. For the particular boundary curves chosen, the asymptotic approximations A involved little more than numerical evaluation of some analytical formulas, once the quadratures had been done analytically.

In general, we found numerically that the lowest- and next-higher-order asymptotic approximations A.0 and A.1 did agree with the lowest-order and refined surface-wave approximations B.0 and B.1, respectively, in their common region of validity. This was true both of the results for the disturbances, and for the phase and group velocities. The agreement improved as the frequency parameter χ was increased, and, for the phase and group velocities, was better between the higher-order and refined approximations than it was between the other two. The asymptotic and surface-wave approximations for the disturbance did not agree particularly well for the case of cylinders with closed boundary curves for values of η for which the disturbance was exponentially small. This was to be expected, since one expression had to suffice for both the lowest-order symmetric and antisymmetric modes in the asymptotic approximation A, while separate expressions were available in the surface-wave approximation B. We also used the refined surface-wave approximation B.1 numerically to describe disturbances in the transition region discussed earlier, and used the lowest-order and refined surface-wave approximations B.0 and B.1 to investigate the higher-order modes.

We turn now to a qualitative description of the numerical results. We first discuss the phenomenon of mode confinement and its dependence upon such things as the shape of the cylinder and the value of the frequency parameter χ. We then discuss our results for the phase and group velocities.

We found that the $\mathbf{t}$ component of the displacement for the lowest-order mode was only a few percent of the size of the $\mathbf{n}$ and $\mathbf{k}$ components. These latter two, when normalized to unity at $\eta = 0$, were either the same as a function of η (asymptotic theory A) or differed by a few percent at most (surface-wave theory B). It thus sufficed to consider a normalized scalar displacement function, rather than a vector function. The complete solution is essentially that for Rayleigh waves traveling on the surface of a plane infinite half space except that it is multiplied by a function of η, which describes the confinement of the wave due to the cylinder curvature, or, to be more precise, the confinement due to the deviation of the cylinder curvature function from a constant value. It is this confinement function (the normalized scalar displacement function) that we computed.

The wedge with a rounded tip and the plane with a ridge on it are cylinders whose cross-sectional boundaries are each described by a curvature function with a single algebraic maximum at $\eta = 0$. For these

cylinders, we found that the confinement function decays rapidly with $|\eta|$ away from its value of unity at $\eta = 0$. This means that the surface-wave disturbance is confined to the vicinity of the tip of the wedge or the ridge on the plane. In both cases, the amount of confinement decreases as the parameter k decreases and the cylinder becomes more nearly planar. For the ridged plane, we observed this when the curvature function was not "almost" constant (i.e., for k not too small). For the wedge, we also made computations for small values of k, corresponding to the flattening out of the wedge into a plane. Here we were aided by an analytical solution of the lowest-order surface wave approximation B.0. It showed that, as $k \to 0$, only the zeroth-order mode exists, that it is symmetric, and that it tends to a Rayleigh wave on a plane infinite half space. This was confirmed by the numerical computations, both in the lowest-order and in the refined surface-wave approximations B.0 and B.1.

We also plotted the confinement functions for higher-order modes on the wedge. For given values of k and the frequency parameter χ, there are finitely many surface modes. The even-order modes are symmetric about $\eta = 0$, and the odd-order modes are antisymmetric.

The ellipse-like rod and bore have boundary curves that are symmetric and which attain their algebraic maxima at two points, $\eta = 0$ and $\eta = \pi$. We investigated only the zeroth-order modes, although higher-order modes may also be studied numerically. The asymptotic approximation A for the zeroth-order mode on a rod or bore actually corresponds to two modes, a symmetric one and an antisymmetric one. These can be treated separately with the surface-wave approximation B. For a cylinder whose curvature is not "almost" constant, we observed confinement of the displacement to two regions. Each cylinder cross-section has two points of maximum algebraic curvature. They define two generators of the cylinder. The displacement is confined in the vicinity of these generators.

We considered the transition from an ellipse-like bore with the definite confinement properties discussed above to a circular bore ($k = 0$), which exhibits no confinement at all. For small values of k, it was necessary to use the refined surface-wave approximation B.1 rather than the lowest-order approximation B.0 in order to describe the modes adequately. We treated the lowest-order symmetric and antisymmetric modes. For $k = 0$, the results agreed with the known analytical results for a circular bore: the confinement function is constant for the symmetric mode and goes like $\cos \eta$ for the antisymmetric mode. As k increased, confinement began to appear. As k approached 0.5, there was definite confinement and the surface-wave approximate results B agreed with the asymptotic results A, which had been obtained earlier and which were valid for curvature functions that were not "almost" constant.

These were the basic confinement properties that we observed when we studied cylinders described by several different cross-sectional curvature functions with a variable parameter k. We also varied the frequency parameter χ and found that, for any given cylinder, the confinement becomes more pronounced as χ increases.

For most of the numerical computations we chose the Poisson ratio to be $\sigma = 0.16974$, corresponding to fused silica. A few computations were made with other values of σ; we found that the confinement increases as σ decreases.

We also calculated the phase and group velocities. In the asymptotic approximation A, these are given by explicit asymptotic formulas. In the surface-wave approximation B, the velocities are given in terms of an eigenvalue and its derivative with respect to χ. The eigenvalue was determined from a periodicity condition in the case of a closed boundary curve and from an appropriate condition at infinity in the case of an open boundary curve. The derivative of the eigenvalue with respect to χ was expressed in terms of quadratures, which were evaluated numerically. This avoided the difficulty of numerical differentiation with respect to the frequency. Both the phase and group velocities tend to the Rayleigh wave velocity as $\chi \to \infty$. We computed the differential phase and group velocities normalized with respect to the transverse-wave velocity c_T.

The trends that we generally observed were that the asymptotic approximations δ_{p2} and δ_{g2} to the differential phase and group velocities agreed roughly with the lowest-order surface-wave approximations δ_{pL} and δ_{gL}. Better agreement was obtained between the next-order asymptotic approximations δ_{p3} and δ_{g3} and the refined surface-wave approximations δ_{pR} and δ_{gR}. The convergence and the agreement improve as the frequency parameter χ increases.

In the transition region between cylinders of constant curvature and those of not "almost" constant curvature (where the parameter k is small and the asymptotic theory is not valid), the lowest-order surface-wave approximation B.0, as expected, was not always too good, particularly for the differential group velocity, so it is necessary to use the refined surface-wave approximation B.1.

Finally, we compared the surface-wave approximation results B for the circular bore with exact theoretical results and obtained excellent agreement.

VI. ACKNOWLEDGMENTS

We are grateful to J. L. Blue and N. L. Schryer for several helpful discussions on some of the numerical procedures, and to R. L. Rosenberg for many helpful suggestions for improving the presentation.

APPENDIX A

We summarize here the asymptotic results[2] in terms of suitably normalized quantities. The longitudinal and transverse velocities are given by $c_L = [(\lambda + 2\mu)/\rho]^{1/2}$ and $c_T = (\mu/\rho)^{1/2}$, where λ and μ are Lamé's constants. Also, the Poisson ratio is $\sigma = \lambda[2(\lambda + \mu)]^{-1}$. The normalized Rayleigh wave velocity is $w_R = c_R/c_T$, where w_R is the root of the equation

$$(1 - \tfrac{1}{2}w_R^2)^4 = (1 - w_R^2)\left[1 - \frac{(1 - 2\sigma)}{2(1 - \sigma)}w_R^2\right], \tag{24}$$

which satisfies $0 < w_R < 1$. We define the quantities

$$b = 1/w_R,\ a_L = \left[b^2 - \frac{(1 - 2\sigma)}{2(1 - \sigma)}\right]^{1/2},\ a_T = (b^2 - 1)^{1/2}, \tag{25}$$

and

$$P = \frac{a_L a_T^2(b^2 - a_L a_T)}{b^2(a_L - a_T)^2 + 2a_L a_T^2(a_L - a_T)} > 0. \tag{26}$$

We further define the quantities R and τ by means of the equations

$$\begin{aligned} 4(a_L - a_T)[b^2(a_L - a_T) + 2a_L a_T^2]R = {} & \frac{P^2(a_L - a_T)^2}{a_L^2 a_T^2}[b^2(a_L + a_T)^2 \\ & - 4a_L^2 a_T^2] + 2P[a_L(b^2 - a_L a_T) - a_T(a_L - a_T)^2] \\ & + [b^2(a_T^2 - 3a_L^2) + 2a_L a_T^3], \end{aligned} \tag{27}$$

and

$$\begin{aligned} (a_L - a_T)[b^2(a_L - a_T) + 2a_L a_T^2](\tau + R) \\ = P\left[\frac{b^2}{a_L a_T}(a_L^3 + a_T^3 - a_L^2 a_T) + a_L a_T(2a_L - 3a_T)\right]. \end{aligned} \tag{28}$$

If η is small, the curvature function $K(\eta)$ has an expansion of the form

$$K(\eta) = d_0 + d_2\eta^2 + d_3\eta^3 + d_4\eta^4 + \cdots. \tag{29}$$

There is no term proportional to η in (29), because our assumption that the curvature attains its algebraic maximum at $\eta = 0$. It is assumed that $d_2 < 0$. We define the quantity

$$Q = \frac{11}{16}\left(\frac{d_3}{d_2}\right)^2 - \frac{3d_4}{4d_2} - \left(\frac{d_0 P}{2b}\right)^2 + d_0^2 R. \tag{30}$$

Then, from the asymptotic results,[2] the reciprocals of the normalized phase and group velocities defined in (11) have the expansions

$$\frac{1}{w_p} = b + \frac{d_0 P}{2b\chi} - \frac{(-d_2 P)^{1/2}}{2b\chi^{3/2}} + \frac{Q}{2b\chi^2} + \cdots, \tag{31}$$

and

$$\frac{1}{w_g} = b + \frac{(-d_2 P)^{1/2}}{4b\chi^{3/2}} - \frac{Q}{2b\chi^2} + \cdots. \tag{32}$$

If we expand the reciprocals of these expansions we obtain those given in (12) and (13).

We now define the functions $C(\eta)$, $F(\eta)$, $G(\eta)$, and $I(\eta)$ occurring in (1). In terms of the curvature function $K(\eta)$, we define

$$I(\eta) = [d_0 - K(\eta)]^{1/2} \operatorname{sgn} \eta, \tag{33}$$

and let

$$L(\eta) = \frac{[K'(\eta) + 2(-d_2)^{1/2} I(\eta)]}{4[d_0 - K(\eta)]}. \tag{34}$$

The prime denotes differentiation with respect to the argument, and it is seen from (29) that $L(0)$ is finite. Then, we define

$$F(\eta) = \exp\left[\int_0^\eta L(\zeta) d\zeta\right], \quad G(\eta) = \int_0^\eta I(\zeta) d\zeta. \tag{35}$$

Next, we let

$$M(\eta) = \int_0^\eta I(\zeta) K(\zeta) d\zeta, \tag{36}$$

and

$$N(\eta) = \int_0^\eta \{L'(\zeta) + [L(\zeta)]^2 - L'(0) - [L(0)]^2\} / I(\zeta) d\zeta. \tag{37}$$

Finally, we define

$$C(\eta) = N(\eta) - d_0 R G(\eta) + \tau M(\eta). \tag{38}$$

Then, from the asymptotic results,[2] the disturbance corresponding to the lowest-order mode can be expressed as

$$\frac{c_T e^{i(\beta z-\omega t)}}{\omega b^{(0)}(0)}\mathbf{u}(\Xi,\eta)$$

$$= F(\eta)\exp\left[-(P\chi)^{1/2}G(\eta)\right]\left(\left[\frac{(b^2+a_T^2)}{2a_T}e^{-a_T\chi\Xi}-a_L e^{-a_L\chi\Xi}\right]\right.$$

$$\times\left[1+\frac{C(\eta)}{2(P\chi)^{1/2}}\right]\mathbf{n}-\left[e^{-a_L\chi\Xi}-\frac{(b^2+a_T^2)}{2b^2}e^{-a_T\chi\Xi}\right]$$

$$\left.\times\left\{\left(\frac{P}{\chi}\right)^{1/2}\mathrm{I}\,(\eta)\mathbf{t}+ib\left[1+\frac{C(\eta)}{2(P\chi)^{1/2}}\right]\mathbf{k}\right\}\right). \quad (39)$$

APPENDIX B

We describe here the "shooting" method used to solve numerically the eigenvalue problems for the refined and lowest-order approximate equations (16) and (19) for the bore and rod, corresponding to the curvature functions $K_1(\eta)$ and $K_2(\eta)$ given by (4) and (5). It is desirable to shoot from $\eta = \pi/2$ to $\eta = 0$, since in the asymptotic region the mode decays exponentially away from $\eta = 0$, and integration from $\eta = 0$ toward $\eta = \pi/2$ would lead to numerical instabilities. Consequently, we let

$$\xi = \pi/2 - \eta,\ Z_1(\xi) = H(\eta),\ Z_2(\xi) = dZ_1/d\xi. \quad (40)$$

Since the eigenvalue ν has to be determined, we also consider the differential equations for

$$Z_3(\xi) = \frac{\partial Z_1}{\partial \nu},\ Z_4(\xi) = \frac{\partial Z_2}{\partial \nu}. \quad (41)$$

The initial conditions are taken as

$$Z_1(0) = 1, \quad Z_2(0) = 0, \quad \text{or } Z_1(0) = 0, \quad Z_2(0) = 1, \quad (42)$$

according to whether the mode is symmetric, or antisymmetric, about $\eta = \pi/2$. In either case, the remaining initial conditions are

$$Z_3(0) = 0, \quad Z_4(0) = 0. \quad (43)$$

An initial guess for the value of ν was made, and the system of equations for $Z_i(\xi)$, $i = 1,2,3,4$, was integrated from $\xi = 0$ to $\xi = \pi/2$. When a mode symmetric about $\eta = 0$ was sought corresponding to $Z_2(\pi/2) = 0$, the initial value of ν was changed to $\nu - Z_2(\pi/2)/Z_4(\pi/2)$, since $Z_2(\pi/2, \nu + \delta) \approx Z_2(\pi/2,\nu) + \delta\partial Z_2/\partial\nu(\pi/2,\nu)$. Analogously, if a mode antisymmetric about $\eta = 0$ was sought, corresponding to $Z_1(\pi/2) = 0$, then the initial value of ν was changed to $\nu - Z_1(\pi/2)/Z_3(\pi/2)$. The process of integrating the system of equations was repeated, until the boundary condition at

$\eta = 0$ was satisfied with sufficient accuracy. The initial iterations were done in single precision, and the final ones in double precision, and only a few iterations were required to obtain the desired accuracy.

The shooting program was checked in the case of the lowest-order approximate equation (19), since the eigenfunctions may be expressed in terms of Mathieu functions[9] when the curvature function is given by (4) or (5). The checks were carried out for values of the parameter $q = P\chi k$ equal to 1, 5, and 10, the eigenvalues and eigenfunctions being checked against tabulated values.[10]

We now turn our attention to the calculation of $d\nu/d\chi$, which is needed to calculate the group velocity from (18). If we let $H_\chi = \partial H/\partial\chi$, then from (16) we obtain

$$\frac{d^2H_\chi}{d\eta^2} + \{\chi[PK(\eta) - 2b\nu] - \nu^2 + \nu SK(\eta) - \tau[K(\eta)]^2\}H_\chi = \left\{[2(b\chi + \nu) - SK(\eta)]\frac{d\nu}{d\chi} + [2b\nu - PK(\eta)]\right\} H(\eta). \quad (44)$$

Hence,

$$\frac{d}{d\eta}\left(H\frac{dH_\chi}{d\eta} - H_\chi\frac{dH}{d\eta}\right) = H\frac{d^2H_\chi}{d\eta^2} - H_\chi\frac{d^2H}{d\eta^2} = \left\{[2(b\chi + \nu) - SK(\eta)]\frac{d\nu}{d\chi} + [2b\nu - PK(\eta)]\right\}[H(\eta)]^2. \quad (45)$$

But from the boundary conditions at $\eta = 0$ and $\eta = \pi/2$, it follows that $[H\,dH_\chi/d\eta - H_\chi\,dH/d\eta]_0^{\pi/2} = 0$. Hence, if we integrate (45) from $\eta = 0$ to $\eta = \pi/2$, we obtain

$$\frac{d\nu}{d\chi}\int_0^{\pi/2}[2(b\chi + \nu) - SK(\eta)][H(\eta)]^2 d\eta = \int_0^{\pi/2}[PK(\eta) - 2b\nu][H(\eta)]^2 d\eta. \quad (46)$$

Analogously, from (19), it follows that

$$2b\chi\frac{d\nu_0}{d\chi}\int_0^{\pi/2}[H_0(\eta)]^2 d\eta = \int_0^{\pi/2}[PK(\eta) - 2b\nu_0][H_0(\eta)]^2 d\eta. \quad (47)$$

The program was written so that the system of equations for $Z_i(\xi)$, $i = 1,2,3,4$, was augmented in the double-precision stage of the iterations to include the evaluation of the two quadratures in (46) or (47).

APPENDIX C

We describe here the "shooting" method, similar to that described in Appendix B, that was used to solve numerically the eigenvalue

problem for the refined approximate equation (16) for the wedge, corresponding to the curvature function $K_3(\eta)$ given by (6). From symmetry, it suffices to consider the interval $\eta \geqq 0$. It is desirable to make a transformation of variables that reduces this interval to a finite one, particularly since we want to integrate from $\eta = \infty$ toward $\eta = 0$, in order to avoid numerical instabilities in the asymptotic region. Consequently, we introduce the new independent variable

$$\zeta = \tfrac{1}{2}(1 - \tanh \eta), \tag{48}$$

which is suggested by the form of the solution (21) of the lowest-order approximate equation (19). This form also suggests the substitution

$$H(\eta) = (\operatorname{sech} \eta)^{\alpha} g(\zeta), \qquad \alpha = (2b\chi\nu + \nu^2)^{1/2} > 0. \tag{49}$$

From (6), (16), (48), and (49), it follows that

$$\zeta(1 - \zeta)\frac{d^2g}{d\zeta^2} + (\alpha + 1)(1 - 2\zeta)\frac{dg}{d\zeta} + [(P\chi + \nu S)k - \alpha(\alpha + 1) - 4\tau k^2\zeta(1 - \zeta)]g = 0. \tag{50}$$

The range of ζ is from 0 to $\frac{1}{2}$, with $\zeta = 0$ corresponding to $\eta = \infty$. Examination of the behavior of the solutions of (50) for $\zeta \to 0$, and the requirement that $H(\eta) \to 0$ as $\eta \to \infty$, lead to the condition that $g(0)$ be finite. The value of $g'(0)$ may be determined by setting $\zeta = 0$ in (50). Thus, as initial conditions, we take

$$g(0) = 1, \qquad g'(0) = \alpha - (P\chi + \nu S)k/(\alpha + 1). \tag{51}$$

Since the eigenvalue ν has to be determined, we also consider the differential equation for $\partial g/\partial \nu$.

Because the coefficient of $d^2g/d\zeta^2$ in (50) vanishes at $\zeta = 0$, we let

$$Y_1 = g - 1, \qquad Y_2 = dY_1/d\zeta - g'(0), \qquad Y_3 = \partial Y_1/\partial \nu, \qquad Y_4 = \partial Y_2/\partial \nu, \tag{52}$$

so that $Y_i(0) = 0$, and $Y_i(\zeta)/\zeta$ is finite at $\zeta = 0$, $i = 1,2,3,4$. The system of equations for $Y_i(\zeta)$ was integrated from $\zeta = 0$ to $\zeta = \frac{1}{2}$, the value of ν being adjusted after each step of the iteration procedure until the condition $g'(\frac{1}{2}) = 0$, or $g(\frac{1}{2}) = 0$, was satisfied with sufficient accuracy. The former condition corresponds to a mode that is symmetric about $\eta = 0$, and the latter to one that is antisymmetric.

It remains to discuss the calculation of $d\nu/d\chi$. If we integrate equation (45) from $\eta = 0$ to $\eta = \infty$, with $K(\eta)$ given by (6), it follows that

$$\frac{d\nu}{d\chi}\int_0^\infty [2(b\chi+\nu)-Sk\,\mathrm{sech}^2\,\eta][H(\eta)]^2 d\eta$$

$$=\int_0^\infty (Pk\,\mathrm{sech}^2\,\eta-2b\nu)[H(\eta)]^2 d\eta. \quad (53)$$

In terms of the new variables given by (48), (49), and (52), this requires the evaluation of the definite integrals

$$\int_0^{1/2}[4\zeta(1-\zeta)]^\alpha[1+Y_1(\zeta)]^2 d\zeta,$$

$$\int_0^{1/2}[4\zeta(1-\zeta)]^{\alpha-1}Y_1(\zeta)[2+Y_1(\zeta)]d\zeta, \quad (54)$$

and the calculation of

$$\int_0^{1/2}[4\zeta(1-\zeta)]^{\alpha-1}d\zeta=\frac{\sqrt{\pi}\Gamma(\alpha)}{4\Gamma(\alpha+\frac{1}{2})}. \quad (55)$$

The integral in (55) was expressed in terms of gamma functions,[11] for which a double-precision routine was available, in order to avoid a singular integrand at $\zeta = 0$ when $0 < \alpha < 1$. The integrals in (54) were evaluated in the double-precision stage of the iterations by augmenting the system of equations for $Y_i(\zeta)$, $i = 1,2,3,4$.

To check the accuracy of the shooting method, the analogous system of equations corresponding to the lowest-order approximate equation (19) was solved numerically, and the results were checked against those calculated from the analytical solution (21) to (23).

REFERENCES

1. J. A. Morrison, "Propagation of High Frequency Surface Waves Along Cylinders of General Cross-Section," J. Math. Phys., *16* (September 1975), pp. 1786–1794.
2. L. O. Wilson and J. A. Morrison, "Propagation of High Frequency Elastic Surface Waves Along Cylinders of General Cross-Section," J. Math. Phys., *16* (September 1975), pp. 1795–1805.
3. J. A. Morrison, "High Frequency Approximations for Elastic Surface Waves Propagating Along Cylinders of General Cross-Section," J. Math. Phys., *17* (June 1976), pp. 958–963.
4. M. A. Biot, "Propagation of Elastic Waves in a Cylindrical Bore Containing a Fluid," J. Appl. Phys., *23* (September 1952), pp. 997–1005.
5. P. Franklin, *Differential and Integral Calculus*, New York: McGraw-Hill, 1953, p. 223.
6. R. L. Rosenberg, R. V. Schmidt, and L. A. Coldren, "Interior-Surface Acoustic Waveguiding in Capillaries," Appl. Phys. Lett., *25* (September 1974), pp. 324–326; also private communication.
7. P. M. Morse and H. Feshbach, *Methods of Theoretical Physics*, Pt. II, New York: McGraw-Hill, p. 1651.
8. M. Abramowitz and I. A. Stegun, *Handbook of Mathematical Functions*, Washington, D. C.: National Bureau of Standards, 1964, p. 556.
9. Ref. 8, pp. 721–750.
10. E. L. Ince, "Tables of the Elliptic Cylinder Functions," Proc. Roy. Soc., Edinburgh, *52* (October 1932), pp. 355–423.
11. Ref. 8, pp. 253–266.